

Building energy-saving potential of a dual-functional solar heating and radiative cooling system

Suhendri Suhendri^a, Mingke Hu^{a,*},¹, Ya Dan^a, Yuehong Su^{a,1}, Bin Zhao^b, Saffa Riffat^a

^a Department of Architecture and Built Environment, University of Nottingham, Nottingham NG7 2RD, United Kingdom

^b Department of Thermal Science and Energy Engineering, University of Science and Technology of China, Hefei 230027, China

ARTICLE INFO

Keywords:

Solar air heater
Radiative cooling
Dual-functional
Building-integrated
Energy-saving potential

ABSTRACT

Space heating and cooling devices that rely on renewable resources are in demand amid energy crises in parts of the world. However, common renewable space heating and cooling devices are mono-functional. For regions with heating and cooling seasons, using two mono-functional devices might double the installation and maintenance costs, and prolong the payback period. This study proposed a dual-functional renewable heating and cooling device by utilising solar power and nocturnal radiative cooling. The device is a modified solar heating (SH) collector that optimises the nocturnal radiative cooling (RC) to become an SHRC collector. Investigation of the SHRC collector's performance and energy-saving potential of a building-integrated SHRC collector was conducted using CFD and EnergyPlus. Analysis of the SHRC collector's performance in various environmental conditions shows that the SHRC collector can reach 42 % thermal efficiency at zero-reduced temperature and > 50 W/m² of net cooling power. Also, studies on the optimal air duct and air gap height reveal that a 1 cm air duct and 4 cm air gap as the best options for the SHRC collector design. Simulations of the building-integrated SHRC with a collector area of 9.43 m² for a typical 100 m² house building demonstrate the multi-seasonal advantage of the SHRC collector, with at least 1.5 kWh more daily savings than the SH and RC collectors in typical winter and summer days. Furthermore, the simulations estimate the annual combined heating and cooling energy savings by the SHRC collector around 32.7 % in Madrid, 25.5 % in Tokyo, and 14.0 % in Isfahan.

1. Introduction

More frequent and severe extreme weather is foreseen as one of the consequences of global warming [1,2]. Just three years after the 2019 heat waves hit European countries, in 2022 another heat wave happened worldwide and in a warmer temperature [3,4]. Hotter temperatures than usual surge the need for cooling in buildings in temperate climate regions [5,6]. With the prediction of a more frequent and hotter heat-wave in the future [1], the temperate climate region may have to readjust its heating system to also support the unaccustomed cooling need.

The conventional heating, ventilating, and air conditioning (HVAC) system can easily provide heating and cooling in one device but consumes a high amount of energy and causes environmental damage [7,8]. The HVAC system is responsible for 63 % of annual energy consumption in a typical EU house [9] and 77 % of the world's fluorinated greenhouse gases emission [10]. Besides the environmental cause, the current

energy crises in Europe and some parts of the world strengthen the economic justification for reducing our reliance on HVAC systems. In this context, renewable space heating and cooling technologies can be the alternative or supplementary solutions to conventional HVAC.

Established renewable space heating techniques usually utilise the heat from the sun such as solar collectors [11,12], solar walls [13,14], or solar windows [15,16]. The working principles of these solar heating devices are substantially the same, i.e., using solar absorptive materials to be heated during the sunlit period. The absorber is protected from convection loss to ambient air using a glass cover so it can yield a warmer temperature. If renewable space heating techniques are mainly sun-based, the sources for renewable space cooling are more diverse. There is a cooling technique via wind convection in the form of a wind catcher in which ambient wind is directed to the indoor environment to promote air movement inside [17,18]. Another way of cooling is via evaporation of water where the ambient air is passed through a water system and cooled by the evaporation of water (hence evaporative cooling) before it enters a building [19,20]. Yet another sustainable

* Corresponding author.

E-mail address: mingke.hu@nottingham.ac.uk (M. Hu).

¹ The two authors have the same contribution to this study.

Nomenclature		ρ	density ($\text{kg}\cdot\text{m}^{-3}$) or reflectivity (-)
c_p	specific heat capacity ($\text{J}\cdot\text{kg}^{-1}\cdot\text{K}^{-1}$)	σ	Stefan-Boltzmann constant ($5.67\times 10^{-8} \text{ W}\cdot\text{m}^{-2}\cdot\text{K}^{-4}$)
E	energy (J)	τ	transmissivity
F	inclination angle factor	$\bar{\tau}$	stress tensor
\vec{F}	external body forces (N)	Abbreviations	
g	gravitational acceleration ($\text{m}\cdot\text{s}^{-2}$)	CFD	computational fluid dynamics
H	solar irradiance ($\text{W}\cdot\text{m}^{-2}$)	DO	discrete ordinates
h	heat transfer coefficient ($\text{W}\cdot\text{m}^{-2}\cdot\text{K}^{-1}$)	PE	polyethylene
k_{eff}	effective thermal conductivity ($\text{W}\cdot\text{m}^{-2}\cdot\text{K}^{-1}$)	RC	radiative cooling
\dot{m}	mass flow rate ($\text{kg}\cdot\text{s}^{-1}$)	RMSD	root mean square deviation
P	fan power (W)	SH	solar heating
p	pressure (Pa)	SHRC	solar heating-radiative cooling
\dot{Q}	volume flow rate ($\text{m}^3\cdot\text{s}^{-1}$)	TMY	typical meteorological year
q	heat flux ($\text{W}\cdot\text{m}^{-2}$)	Subscript	
S_m	mass source term ($\text{kg}\cdot\text{s}^{-1}$)	a/e	absorber/emitter
S_h	energy source term (W)	ad	air duct
T	temperature ($^{\circ}\text{C}$)	ag	air gap
t	time (s)	amb	ambient
v	air velocity ($\text{m}\cdot\text{s}^{-1}$)	cov	cover
Greek letters		ins	insulation
α	absorptivity	rad	radiation
ε	emissivity	sol	solar
η_{th}	thermal efficiency (%)	the	thermal

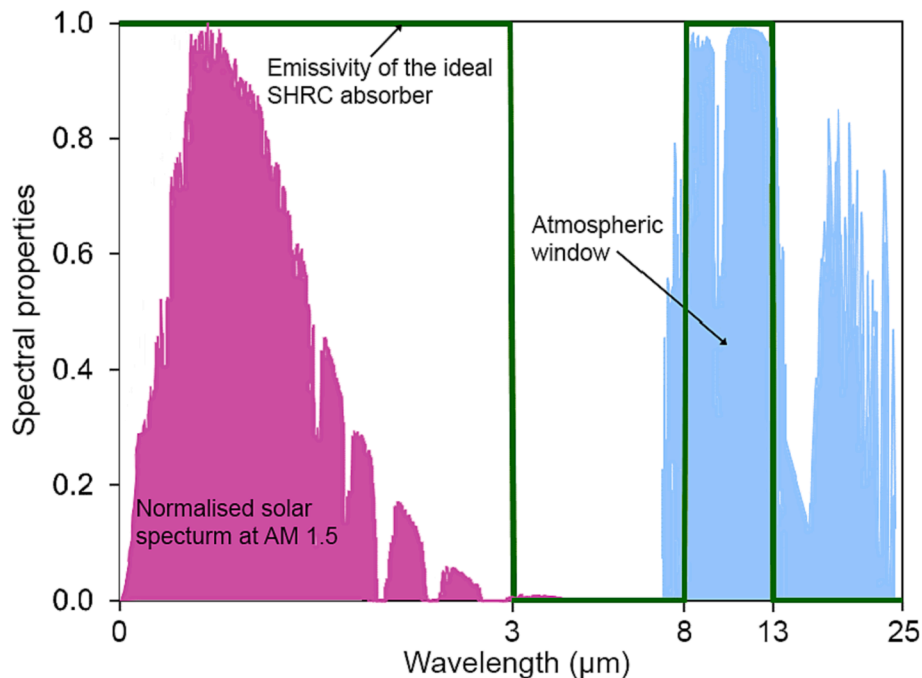


Fig. 1. The ideal spectral properties of the SHRC absorber.

cooling method is radiative cooling (RC) which dissipates heat to the cold sky via thermal radiation to cool the building envelope directly or thermal carriers [21,22]. RC occurs due to a high transmissivity of the sky in the infrared band of 8–13 μm (the atmospheric window) so heat from any terrestrial body can be radiated to outer space.

However, the previously mentioned renewable heating and cooling systems usually come as separate devices. A solar collector delivers heat only and is idle at night. Meanwhile, a building's heating and cooling

demands vary throughout the year depending on the season. This means that the solar collector is useful only for the heating season, and the building should have another cooling device for the cooling season. This can be costly for installation and maintenance. Therefore, a device that offers both renewable space heating and cooling would be more seasonally adaptive and more cost-effective in these two aspects [23].

The solar collector is possible to be such a device if the absorber and glass cover of the collector are modified accordingly. The absorber of a

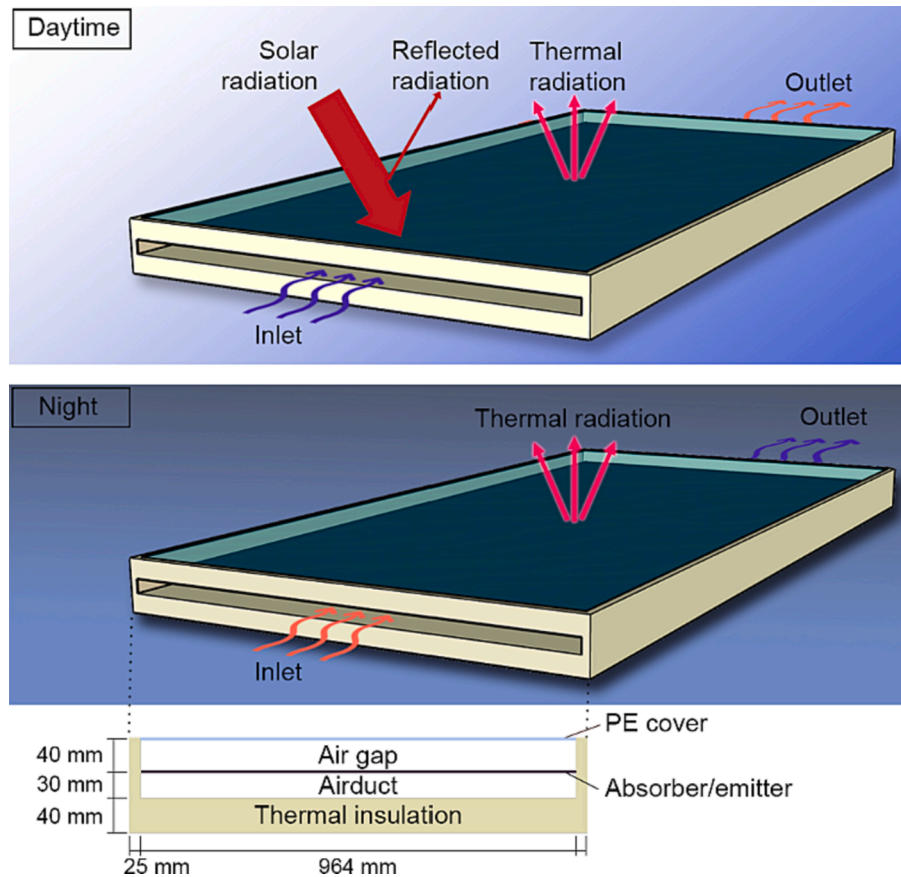


Fig. 2. Illustration of the air-based SHRC collector.

solar collector has very high absorptivity in the solar band (0.2–3 μm) but low emissivity in other radiation bands. If the absorber is made to be emissive in the atmospheric window band (8–13 μm), it also can be employed as a nocturnal RC emitter. Fig. 1 illustrates the characteristics of the spectral properties of an ideal solar heating-radiative cooling (SHRC) absorber/emitter. Moreover, the glass cover that prevents the SH absorber surface from convective heat loss is transparent for solar radiation but opaque for infrared radiation and thus blocks the surface’s radiation to the sky. For this reason, the cover must also be changed with a material that has high transmissivity in both solar and atmospheric window bands, usually a polyethylene (PE) film [24,25].

This study evaluates the heating and cooling performance of the dual-functional SHRC collector in a yearly period to reveal the adaptability of the collector in different seasons compared to the monofunctional solar heating (SH) and RC collectors. Effects of various environmental, structural, and operational conditions on the collector performance are also assessed. In addition to that, this paper also estimates the energy-saving potential of the SHRC collector when installed onto a building roof. The study employs computational fluid dynamics (CFD) and EnergyPlus simulations. A case study building is chosen from the test house of the International Energy Agency’s (IEA) Energy in

Buildings and Communities (EBC) programme (IEA-EBC Annex 58) [26]. Three cities, each with different climate types, are selected to be the case study locations.

2. Design of the air-based solar heating and radiative cooling (SHRC) system

2.1. The SHRC collector

Like the conventional solar collector, the SHRC collector consists of an absorber/emitter, a convection cover, and insulation. The absorber/emitter with a dimension of 1960 mm in length, 964 in width, and 0.4 mm in thickness, sits between a 40 mm air gap above and a 30 mm air duct below. Atop the air gap is the convection cover of PE film with a thickness of 6 μm. Additionally, a 40 mm insulation board is placed under the air duct. Insulation also surrounds the side of the air gap and the air duct, with a thickness of 25 mm. The air inlet and outlet are positioned at the ends of the air duct. The illustration of the module is seen in Fig. 2. The SHRC collector material is based on Zhao et al. [27], it has an absorptivity of 0.92 in the solar radiation band and an emissivity of 0.84 in the atmospheric window band. Other thermal and spectral

Table 1
Thermal and spectral properties of the materials.

Material	Thermal properties			Absorptivity/emissivity			
	Thermal conductivity (W·m ⁻¹ ·K ⁻¹)	Density (kg·m ⁻³)	Specific heat capacity (J·kg ⁻¹ ·K ⁻¹)	0.2–3 μm	3–8 μm	8–13 μm	13–25 μm
SH absorber	202.4	2719	871	0.92	0.17	0.09	0.06
RC emitter				0.04	0.27	0.78	0.59
SHRC absorber/emitter				0.92	0.51	0.84	0.54
PE film	0.45	910	1900	0.05	0.05	0.05	0.05
Insulation board	0.042	38	1400	0.70	0.90	0.90	0.90

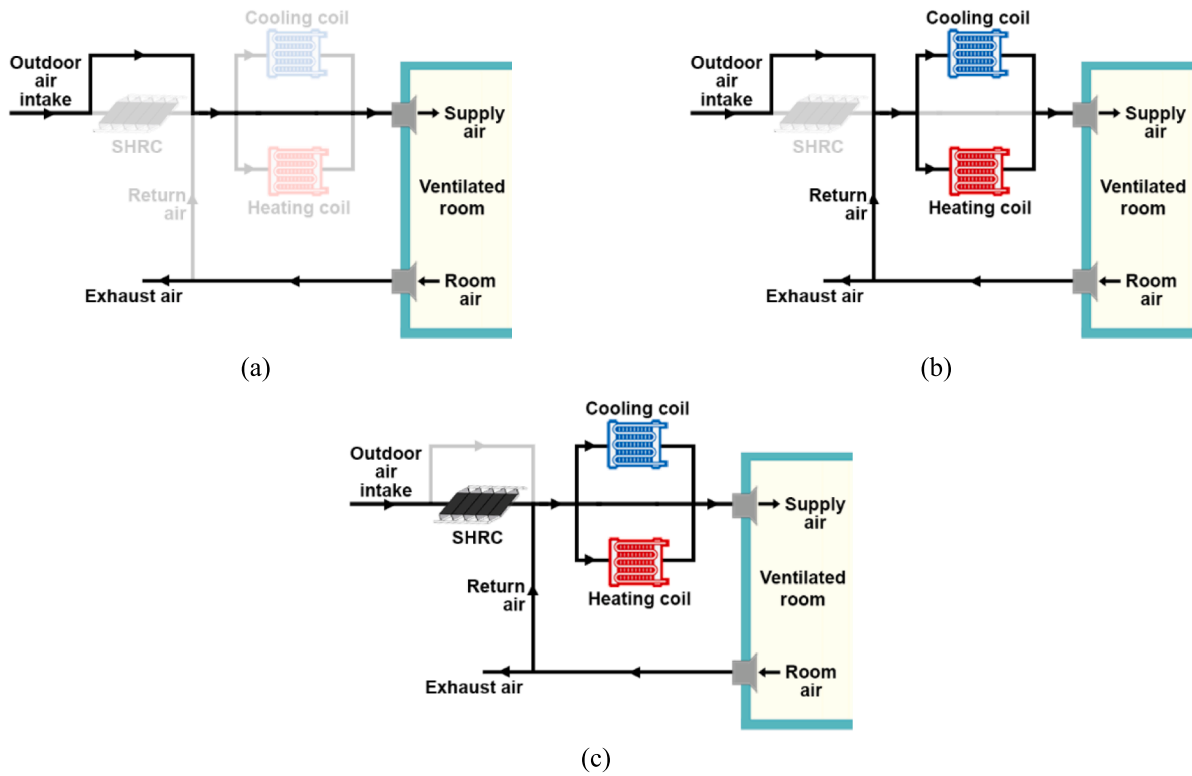


Fig. 3. Schematic diagram of the SHRC-assisted HVAC system: (a) fan ventilation mode, (b) HVAC mode, and (c) SHRC-HVAC mode.

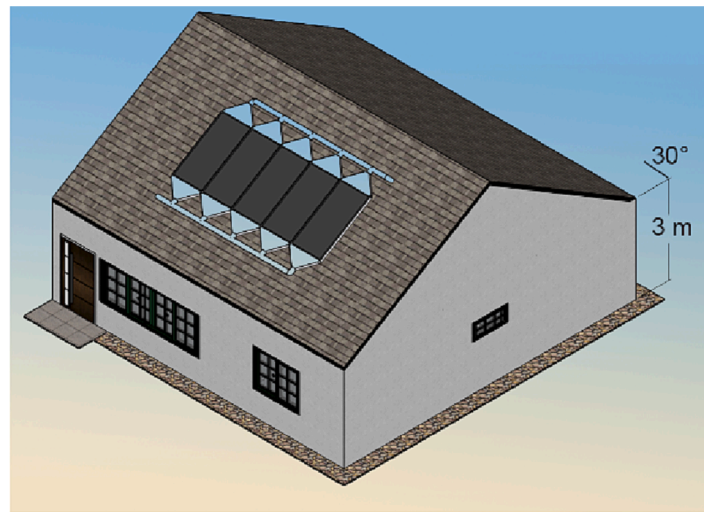
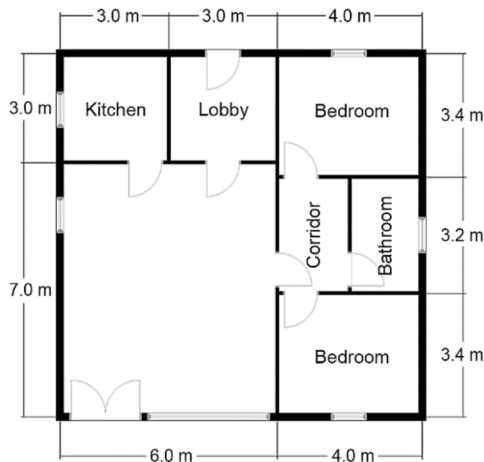


Fig. 4. Illustration of the building-integrated SHRC collector applied in the case study building.

properties of the materials of the collector are detailed in Table 1. For comparison, the conventional SH absorber [28] and RC emitter [29] are also included in Table 1.

2.2. The building-integrated SHRC collector

One way to integrate the SHRC collector into buildings and utilise its heating and cooling energy provided by the collector is through integration with a conventional HVAC system. Fig. 3 shows three possible working modes of the system. In the first mode, if the outdoor air is in the comfortable temperature range, then it is directly drawn into the

room and the room air is directly exhausted outside (Fig. 3a). The second working mode is the HVAC-only mode, i.e., when the outdoor air needs to be heated but the SHRC collector provides cooling or vice versa (Fig. 3b). This condition occurs, for instance, in the winter nights or summer noon. The third mode is when the SHRC collector assists the HVAC system by being a precooling or preheating device to the outdoor air (Fig. 3c). It is in the third mode that the SHRC collector contributes to the energy saving of buildings.

To analyse the energy-saving potential of the building-integrated SHRC collector, a case study building was chosen. The building is a single-story test house developed by IEA-EBC Annex 58 [26], with a

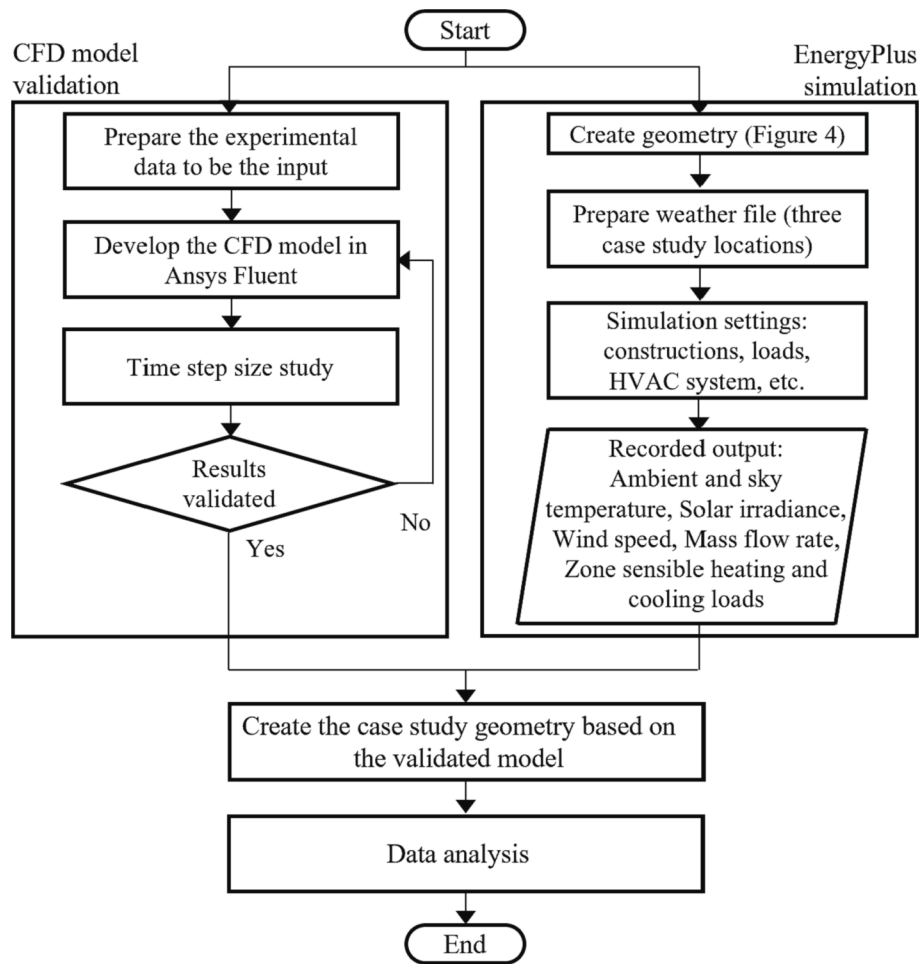


Fig. 5. Flow diagram of the research methodology.

south-facing facade, a 10 m by 10 m floor plan, and 1 living room, 2 bedrooms, 1 kitchen, and 1 bathroom. All rooms have window access to the outdoor environment. Fig. 4 visualises the case study building with the integrated SHRC collector on the roof. Five SHRC collectors are connected in parallel with a total area of 9.43 m² to supply the pre-heated or pre-cooled air accordingly.

3. Methodology

To assess the energy-saving potential of a building-integrated SHRC system, this study used two simulation methods: CFD and EnergyPlus.

The CFD simulations were used to model the performance of the SHRC collector, while EnergyPlus was used to simulate the annual heating and cooling loads of the case study building. The flow chart in Fig. 5 outlines the steps involved in the simulations, which include using the validated CFD model of the SHRC collector with input data from the EnergyPlus simulation. Additionally, the energy-saving potential of the SHRC system was analysed by comparing the results from the CFD simulation with the heating and cooling loads data from EnergyPlus. By combining these two simulation methods, the study provides a comprehensive evaluation of the performance and energy-saving potential of the SHRC collector.

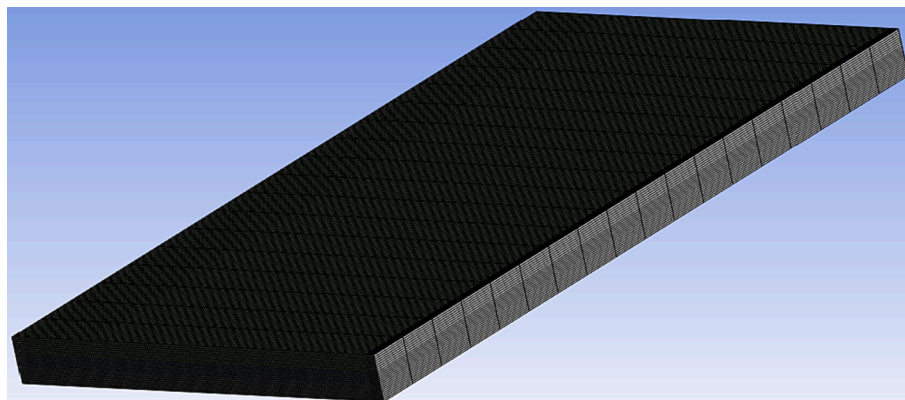


Fig. 6. Illustration of the 5 mm mesh size swept across the SHRC collector geometry.

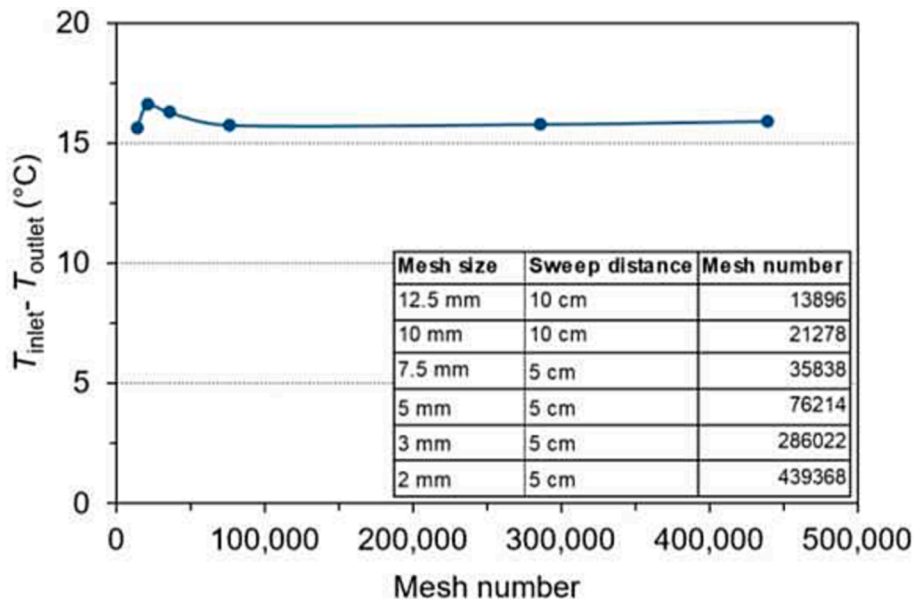


Fig. 7. Illustration of the 5 mm mesh size swept across the SHRC collector geometry.

3.1. CFD model of the SHRC collector

Ansys Fluent numerically solves the transport equations for CFD simulation, namely the continuity, momentum, and energy equations, as expressed in Eqs. (1) to (3) [30]. In Eq. (1), ρ and v terms are the air density and velocity respectively, while t is time, and S_m is the mass addition to the system.

$$\frac{\partial \rho}{\partial t} + \nabla \cdot (\rho v) = S_m \tag{1}$$

Additionally, Eq. (2) which represents the momentum equation accounts for the relation between the static pressure (p), total stress on the fluid body (summed up in the stress tensor ($\bar{\tau}$)), the gravitational body force (ρg), and the external body forces (\vec{F}).

$$\frac{\partial}{\partial t}(\rho v) + \nabla \cdot (\rho v v) = -\nabla p + \nabla \cdot (\bar{\tau}) + \rho g + \vec{F} \tag{2}$$

Also, the energy equation in Eq. (3) accounts for the total energy of the fluid (E), the effective conductivity of the fluid (k_{eff}), and the fluid temperature (T). Any additional energy input to the system is included in S_h in Eq. (3).

$$\frac{\partial}{\partial t}(\rho E) + \nabla \cdot (v(\rho E + p)) = \nabla \cdot (k_{eff} \nabla T + (\bar{\tau}_{eff} \cdot v)) + S_h \tag{3}$$

To accurately model the performance of the SHRC collector, a geometry model was created based on its dimensions, as shown in Fig. 2.

The geometry was then discretised using a structured hexahedral mesh, with a maximum mesh size of 5 mm swept along the computational domain with a 5 cm distance. The meshing result is shown in Fig. 6. This mesh size is selected after the mesh-independence study indicating its reliability in giving a grid-independent simulation result, as summarised in Fig. 7. As seen in Fig. 7, the simulation starts to give a stable result from the 5 mm mesh size (mesh number 76214).

Further, for the simulation settings, the Laminar flow model Standard $k-\epsilon$ turbulence model was employed, along with the discrete-ordinate (DO) radiation model for radiation modelling due to its capability to account for the non-grey model [31]. To run the solver, the Coupled algorithm for pressure-velocity coupling was used, along with the PRESTO! discretisation scheme for the pressure terms. Throughout the simulation, results were monitored by tracking residuals and key parameters, such as outlet air temperature, pressure, and specific heat capacity.

Moreover, the boundary conditions of the SHRC collector were developed based on the heat-balanced model of the collector as shown in Fig. 8. Firstly, the heat balance of the PE cover is summarised by Eq. (4). The cover receives radiation from the sun ($q_{sol-cov}$), as well as exchanged heat via radiation with the atmosphere and the SHRC absorber/emitter below (q_{rad}), and via convection with the ambient air (q_{wind}) and the air gap (q_{ag-cov}). On the right side of Eq. (4), the transient term is introduced with d_{cov} as the PE cover's thickness. To be more detailed, each heat transfer component is defined in subsequent equations.

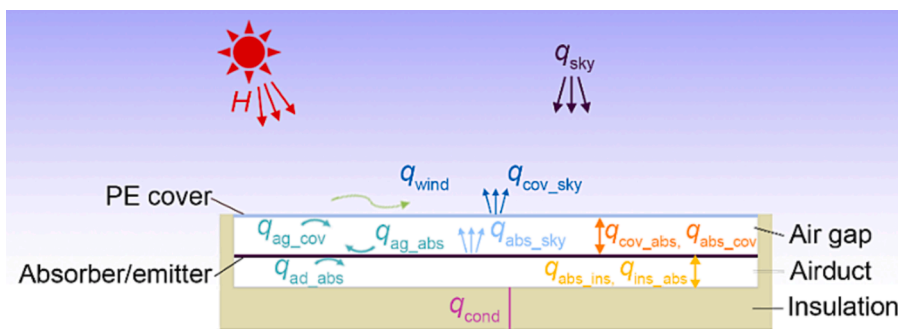


Fig. 8. Heat balance of the SHRC collector.

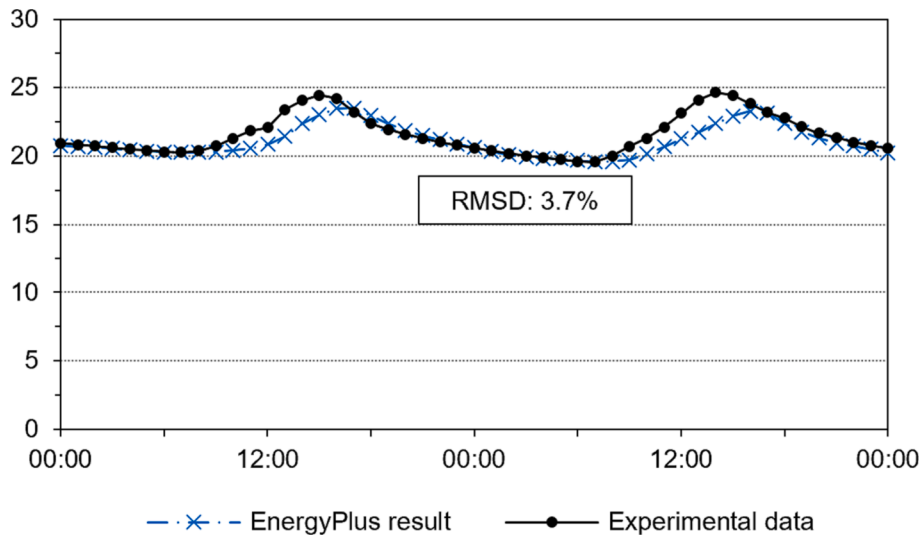


Fig. 9. EnergyPlus model validation.

$$q_{\text{sol-cov}} + q_{\text{rad}} + q_{\text{wind}} + q_{\text{ag-cov}} = \begin{cases} 0, \text{ steady state} \\ \rho c_{p_{\text{cov}}} d_{\text{cov}} \frac{\partial T_{\text{cov}}}{\partial t}, \text{ transient state} \end{cases} \quad (4)$$

In Eq. (5), $q_{\text{sol-cov}}$ is the amount of solar radiation that is absorbed by the cover, with α_{cov} being the PE cover's absorptivity, and H is the total solar irradiance that falls onto the cover.

$$q_{\text{sol-cov}} = \alpha_{\text{cov}} H \quad (5)$$

Thermal radiation, q_{rad} , describes the balance between incoming radiation from the sky (q_{sky}) and the absorber/emitter ($q_{\text{a/e-cov}}$), as well as the outgoing radiation from the cover upward ($q_{\text{cov-sky}}$) and downward ($q_{\text{cov-a/e}}$) (see Eq. (6)). The cover-atmosphere radiative heat exchange is represented in Eq. (7) with F as the inclination angle effect of the thermal radiation power to the sky [32], ϵ_{cov} as the PE cover's emissivity in the atmospheric window band, σ as Stefan-Boltzmann constant, T_{sky} as the sky temperature, and T_{cov} is the PE cover's temperature. Note that for the energy saving analysis, the sky temperature was taken from the typical meteorological year (EnergyPlus TMY) weather data, while for the parametric studies, it was calculated from Eq. (8) [33] and Eq. (9) [34]. Moreover, the cover-absorber radiation exchange is internally calculated by Ansys.

$$q_{\text{rad}} = (q_{\text{sky}} - q_{\text{cov-sky}}) + (q_{\text{a/e-cov}} - q_{\text{cov-a/e}}) \quad (6)$$

$$q_{\text{sky}} - q_{\text{cov-sky}} = F \epsilon_{\text{cov}} \sigma (T_{\text{sky}}^4 - T_{\text{cov}}^4) \quad (7)$$

$$\epsilon_{\text{sky}} = 0.754 + 0.0044 T_{\text{dp}} \quad (8)$$

$$T_{\text{sky}}^4 = \epsilon_{\text{sky}} T_{\text{amb}}^4 \quad (9)$$

Further, the q_{wind} represents convection heat transfer due to ambient wind (Eq. (10)), with the formula for heat transfer coefficient (h_{wind}) shown in Eq. (11) [35]. In Eq. (10), T_{amb} represents the ambient temperature, and in Eq. (11), v denotes wind speed. Lastly, the convection heat transfer with the air gap ($q_{\text{ag-cov}}$) in Eq. (4), is internally calculated by Ansys Fluent.

$$q_{\text{wind}} = h_{\text{wind}} (T_{\text{amb}} - T_{\text{cov}}) \quad (10)$$

$$h_{\text{wind}} = 2.8 + 3.0v \quad (11)$$

The second in the heat balance equation for the SHRC collector is for the absorber/emitter (Eq. (12)). The absorber/emitter receives part of the solar radiation that is transmitted by the PE cover. Some of that solar

radiation is reflected back-and-forth between the absorber/emitter and the PE cover. Eq. (13) sums the solar radiation absorbed by the absorber/emitter ($q_{\text{sol-a/e}}$) where τ_{cov} is the PE cover's solar transmissivity, $\alpha_{\text{a/e}}$ is the solar absorptivity of the absorber/emitter, ρ_{cov} and $\rho_{\text{a/e}}$ are the solar reflectivity of the cover and the absorber/emitter respectively.

$$q_{\text{sol-a/e}} + q_{\text{rad}} + q_{\text{ag-a/e}} + q_{\text{ad-a/e}} = \begin{cases} 0, \text{ steady state} \\ \rho c_{p_{\text{a/e}}} d_{\text{a/e}} \frac{\partial T_{\text{a/e}}}{\partial t}, \text{ transient state} \end{cases} \quad (12)$$

$$q_{\text{sol}} = \frac{\tau_{\text{cov}} \alpha_{\text{a/e}}}{(1 - \rho_{\text{cov}} \rho_{\text{a/e}})} H \quad (13)$$

Another heat transfer term in Eq. (12), q_{rad} , is the radiation heat exchange between the absorber/emitter with the sky (represented by $q_{\text{sky}} - q_{\text{a/e-sky}}$ in Eq. (14)), the cover ($q_{\text{cov-a/e}} - q_{\text{a/e-cov}}$), and the back insulation ($q_{\text{ins-a/e}} - q_{\text{a/e-ins}}$). The latter two radiative heat exchanges are internally calculated by Ansys, whereas the absorber-sky radiation exchange is calculated using Eq. (15), which is an adjusted version of Eq. (6) to account for the infrared transmissivity of the PE cover (τ_{cov}). Lastly, convection heat transfer with the air gap ($q_{\text{ag-a/e}}$) and the air duct ($q_{\text{ad-a/e}}$) in Eq. (12) are internally calculated by Ansys Fluent. The $q_{\text{ad-a/e}}$ is dependent on the mass flow rate of air in the air duct.

$$q_{\text{rad}} = (q_{\text{sky}} - q_{\text{a/e-sky}}) + (q_{\text{cov-a/e}} - q_{\text{a/e-cov}}) + (q_{\text{ins-a/e}} - q_{\text{a/e-ins}}) \quad (14)$$

$$q_{\text{sky}} - q_{\text{a/e-sky}} = F \tau_{\text{cov}} \epsilon_{\text{a/e}} \sigma (T_{\text{sky}}^4 - T_{\text{a/e}}^4) \quad (15)$$

3.2. EnergyPlus simulation setup

Before the case study building was simulated in EnergyPlus for energy-saving analysis, the EnergyPlus model of the building was first validated against the experimental data of the IEA-EBC Annex 58 building [36]. The experiment on the building (see Fig. 4) was done in Munich, Germany (48.1° N, 11.6° E), measuring the indoor temperatures of all rooms when the heat load from two heaters were applied. The construction materials of the EnergyPlus model were set according to the detail given by Strachan et al. [36]. Fig. 9 below compares the indoor temperature of the living room from the simulation and the experimental data. The figure shows a good agreement between the simulation and the experiment with an average difference of 0.5 °C and RMSD of 3.7 %.

Further, the calibrated EnergyPlus model was used in the energy-saving analysis of the building-integrated SHRC system in three case

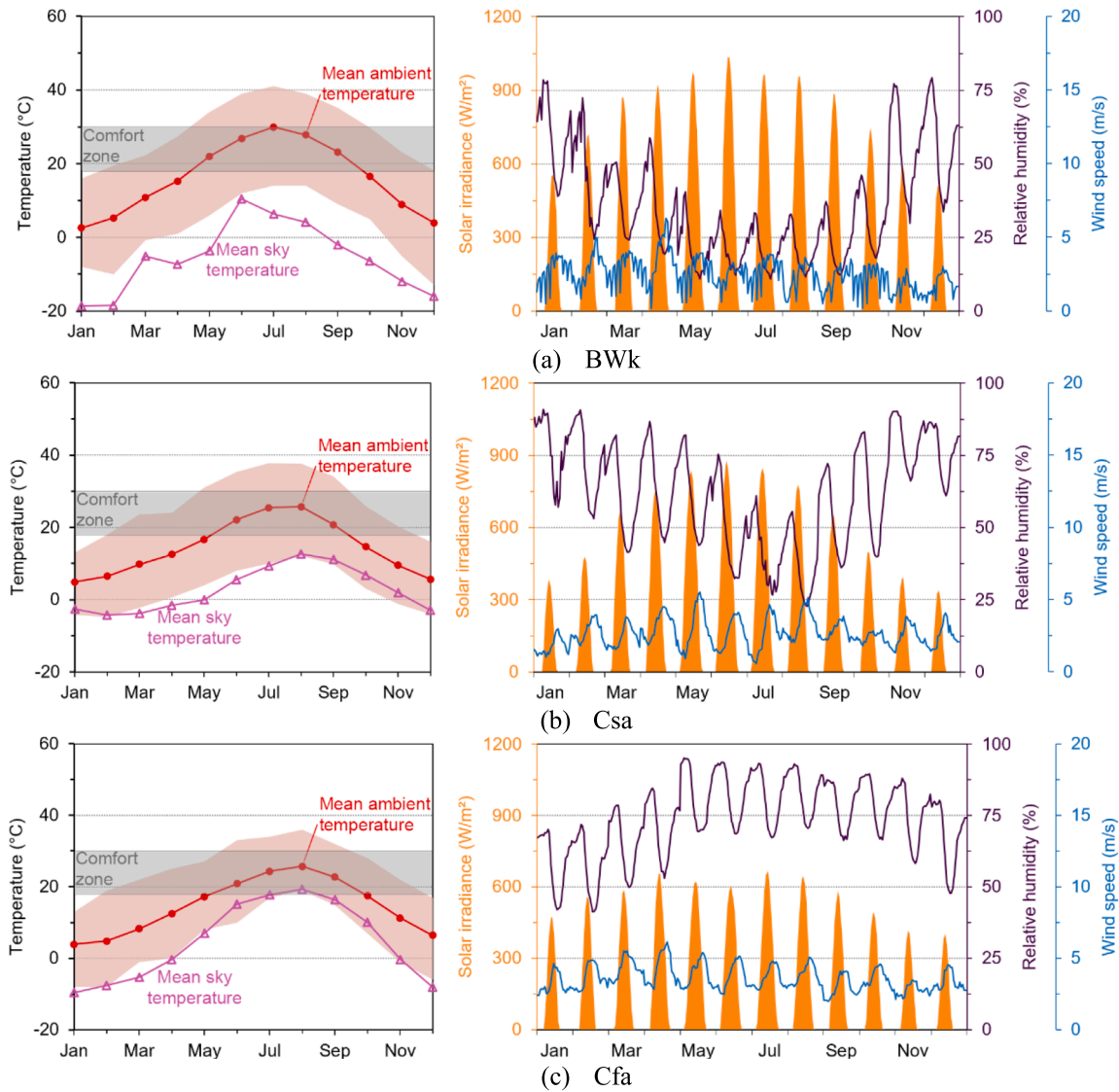


Fig. 10. Dry bulb temperature data for (a) Isfahan, Iran; (b) Madrid, Spain; and (c) Tokyo, Japan [39,40].

study locations. The locations were chosen to assess the most appropriate climate condition for the SHRC collector among the climate types that have heating and cooling seasons. Based on the Koppen-Geiger climate classification [37], the three climate types are: the cold desert climate (BWk), represented by Isfahan, Iran; the hot summer Mediterranean climate (Csa) represented by Madrid, Spain; and the humid subtropical climate (Cfa) represented by Tokyo, Japan. Fig. 10 illustrates the ambient temperature variations in these locations, which indicate a need for space heating and cooling, as the outdoor temperature variations lie outside the adaptive thermal comfort zone [38]. In addition, Fig. 10 shows that Isfahan and Madrid with dry climates and low relative humidity levels, have a higher potential for radiative sky cooling due to the larger gap between the ambient and sky temperature, and thus a high potential for radiative sky cooling.

Furthermore, the set point temperatures for space heating and cooling were set at 21 °C and 24 °C respectively. The heating and cooling supply air temperatures were 40 °C and 18 °C respectively, provided by the selected HVAC system with a gas heating coil with an efficiency of 0.9 and a direct expansion cooling coil (single speed) with a rated COP of 3.6 [41]. The ambient and sky temperature, solar irradiance, wind speed, and mass flow rate data were obtained from these EnergyPlus simulations [39,42]. Besides those parameters, the simulations also reported the heating and cooling loads for each case study location. These

data were then used in the analysis of the energy-saving potential of the SHRC collector, by comparing it with the heating and cooling energy yield data from CFD simulations.

3.3. Performance evaluation of the SHRC collector

The SHRC collector performance is measured using three indicators, namely the outlet temperature, the heating/cooling power, as well as the thermal efficiency. The outlet temperature data are obtained through the CFD simulations, while the heating/cooling power ($q_{\text{heating/cooling}}$) is calculated using Eq. (16) below.

$$q_{\text{heating/cooling}} = (\dot{m}_p(T_{\text{outlet}} - T_{\text{in}}) - P) / A \quad (16)$$

Moreover, the thermal efficiency (η_{th}) is calculated using Eq. (17), where A in Eq. (16) is the collector's area. Considering the energy used by the fan, Eq. (15) includes the ideal fan power consumption in the form of $P = \Delta p \bullet \dot{Q}$, with Δp as the pressure drop across the air duct (Pa) and \dot{Q} as the volumetric flow rate of the air (m^3/s).

$$\eta_{\text{th}} = q_{\text{heating}} / H \quad (17)$$

Sensitivity analyses were conducted using a one-day CFD simulation of the typical summer day of Isfahan, to assess the effect of various key

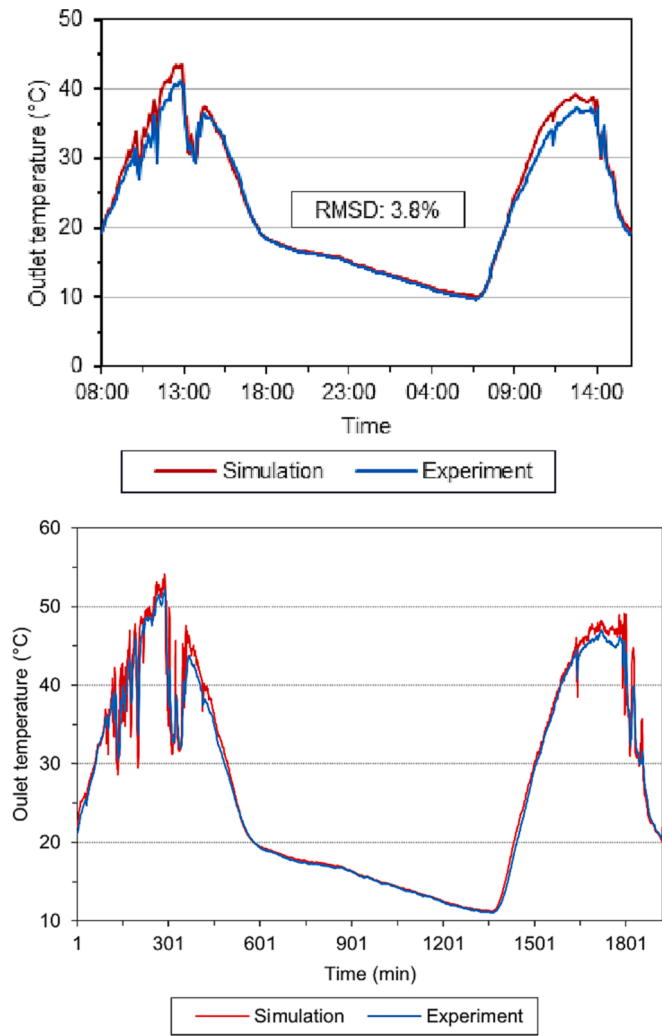


Fig. 11. Comparison between simulation results from the CFD model and experimental data from Hu et al. [28].

parameters on the collector’s performance. Moreover, for the energy-saving analysis of the building-integrated SHRC collector, one-year transient CFD simulations in ANSYS were conducted to get the hourly outlet air temperature for the whole simulation year. From the one-year simulations, the heating and cooling energy yields, $E_{\text{heating/cooling}}$ (Wh), were calculated using the formula in Eq. (18) below, with A_{total} is the total area of the SHRC collector’s array, and t is the simulation’s time step size. Note that, t is the optimal time step size based on the time step independence study.

$$E_{\text{heating/cooling}} = q_{\text{heating/cooling}} A_{\text{total}} t \quad (18)$$

It is anticipated that the time in which the heating/cooling load arises does not match the time in which the heating/cooling energy yielded. Therefore, the analysis of the energy-saving potential of the SHRC collector also accounts for the time matching between the yield energy and the load conditions (supply-demand matching). For a given period, one can calculate the percentage of matched time using Eq. (19) below. Then, it follows that the energy saved by implementing the SHRC collector is the product of energy yield multiplied by the percentage of the matched time.

$$\% \text{ of matched time} = \frac{\text{Matched hours between energy yield \& load}}{\text{Total hours of energy yield}} \times 100\% \quad (19)$$

3.4. Model validation and sensitivity analysis

To validate the CFD model, results from the simulations were compared to the experimental data from Hu et al. [28]. The SH collector measured by Hu et al. [28] has the same dimension and structure as the SHRC collector in this study, but the measured data available were for the conventional SH only. Thus, for validation, the CFD simulation modelled the SH collector in the experiment using transient simulation with a time step size of 60 s (1 min). As seen in Fig. 11 below, there is a good agreement between the CFD model and the experiment. The root mean square deviation (RMSD) assessment using the formula in Eq. (20), where $X_{\text{sim},i}$ is the simulation data point and $X_{\text{exp},i}$ is the experimental data point [43], showing good conformity between the two. The RMSD of the simulated outlet temperature is 43.8 %.

$$RMSD = \sqrt{\frac{1}{n} \sum_{i=1}^n \left[\frac{(X_{\text{sim},i} - X_{\text{exp},i})}{X_{\text{exp},i}} \right]^2} \quad (20)$$

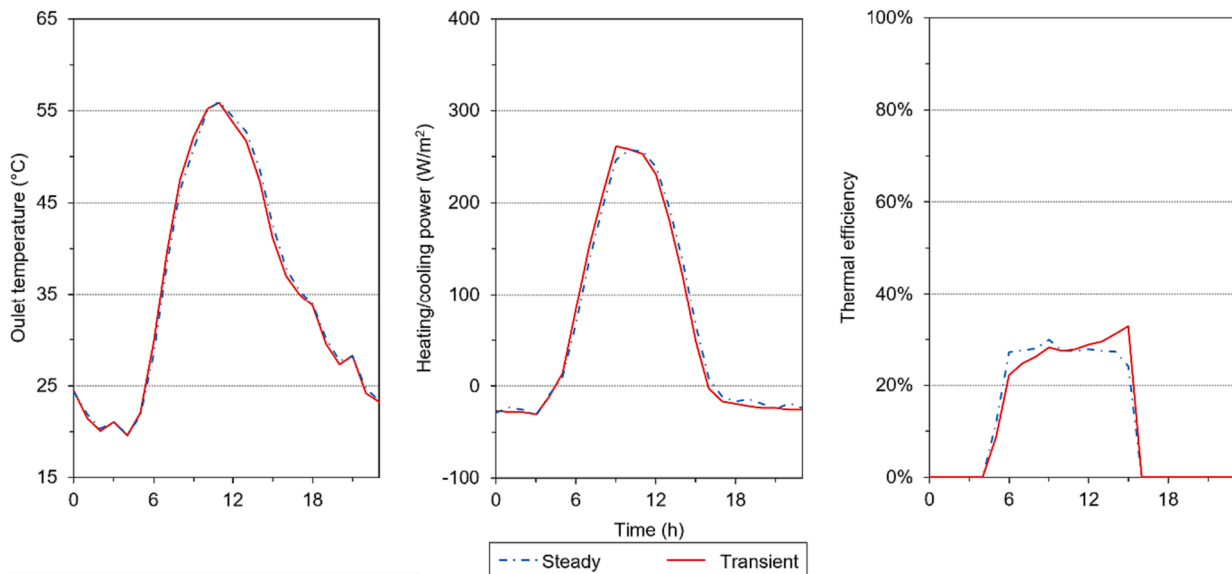


Fig. 12. Comparison between the results from the steady and transient CFD simulations for the SHRC collector ($\dot{m} = 0.023$ kg/s).

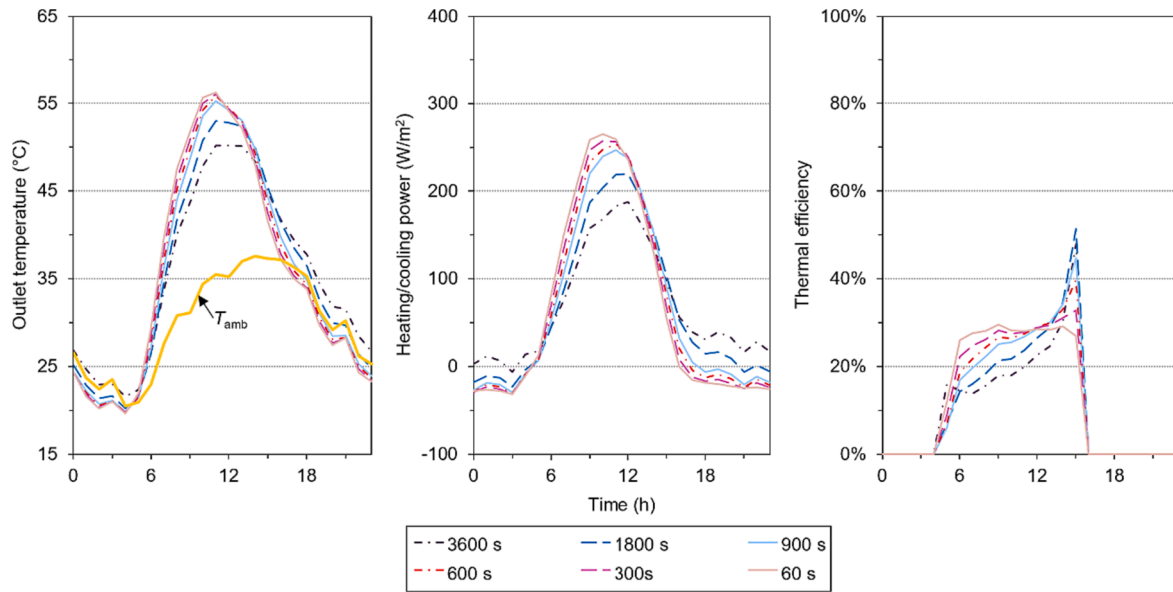


Fig. 13. Effect of time step sizes on the SHRC collector's performance ($\dot{m} = 0.023 \text{ kg/s}$).

a. Differences between steady and transient simulation results.

The differences between the results from steady and transient simulations are also worth analysing. The steady simulation will not be used for the annual energy saving analysis, yet it is useful in the study of the effect of various environmental conditions on the SHRC performance. Comparing the results from the two simulation models can give an overview of the differences between them and whether they can be used interchangeably. Fig. 12 compares the steady simulation results with the transient simulation with 300 s time step size using the typical summer day data of Isfahan. It can be seen from the figure that the results from the steady simulation are close to the transient one, with an RMSD of 1.9 %. Thus, principally the two can be used interchangeably. However, for practical reasons, the steady simulation will be used for the analysis of the effect of various environmental conditions on the SHRC performance, while the transient simulation is used for the annual simulation.

b. Effect of time step size.

A large time step size may not be reliable for a transient simulation, but a very fine time step size is time-consuming and resource intensive. Fig. 13 summarises the results from one-day transient simulations, using the typical summer day data of Isfahan, with several time step sizes. It is seen in Fig. 13 that the time step of 900 s (15 min) or larger results in not reliable outlet temperature, and thus gives unreliable power and thermal efficiency as well. RMSDs of the 3600 s, 1800 s, and 900 s to the 60 s time step sizes are 12.2 %, 7.9 %, and 4.4 % respectively. The large time step sizes, especially the 3600 s and the 1800 s, underestimate the heating effect during daytime and the cooling effect at nighttime (see Fig. 13). The intended RC effect is not observed when using the $\geq 1800 \text{ s}$ time step size. This is because the simulation with a large time step size does not fully develop into a stable condition in the hourly weather data. This is apparent in the thermal efficiency plotting in Fig. 13, the larger time step sizes show sudden changes in the afternoon (around 3p.m.),

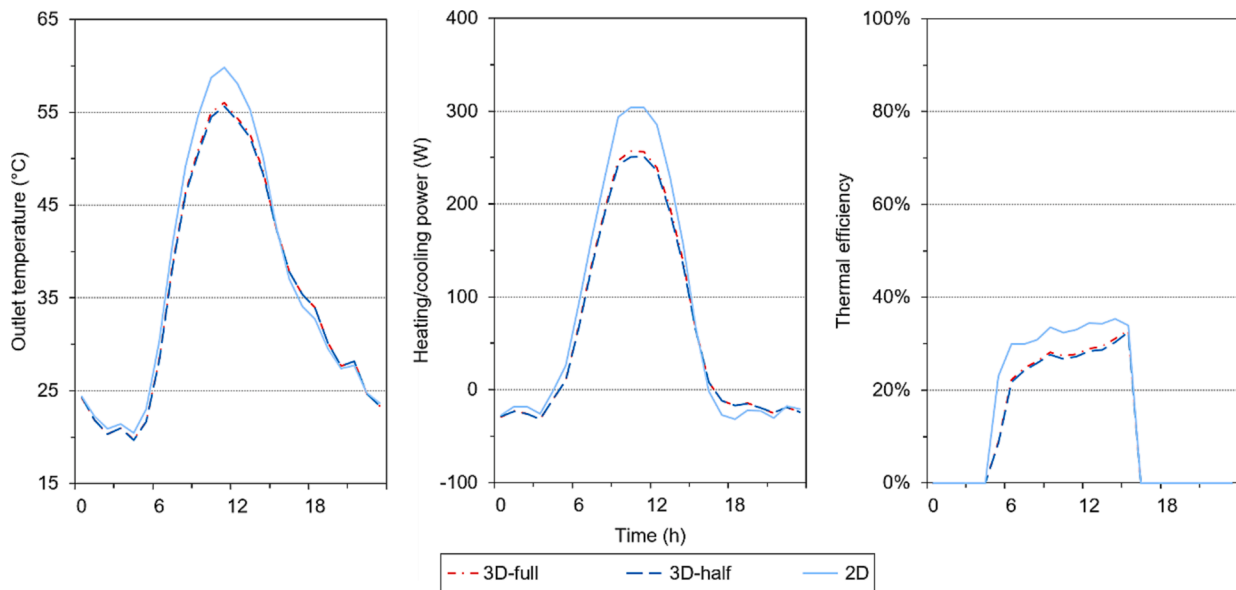


Fig. 14. Effect of the CFD geometry model on the SHRC collector's performance ($\dot{m} = 0.023 \text{ kg/s}$).

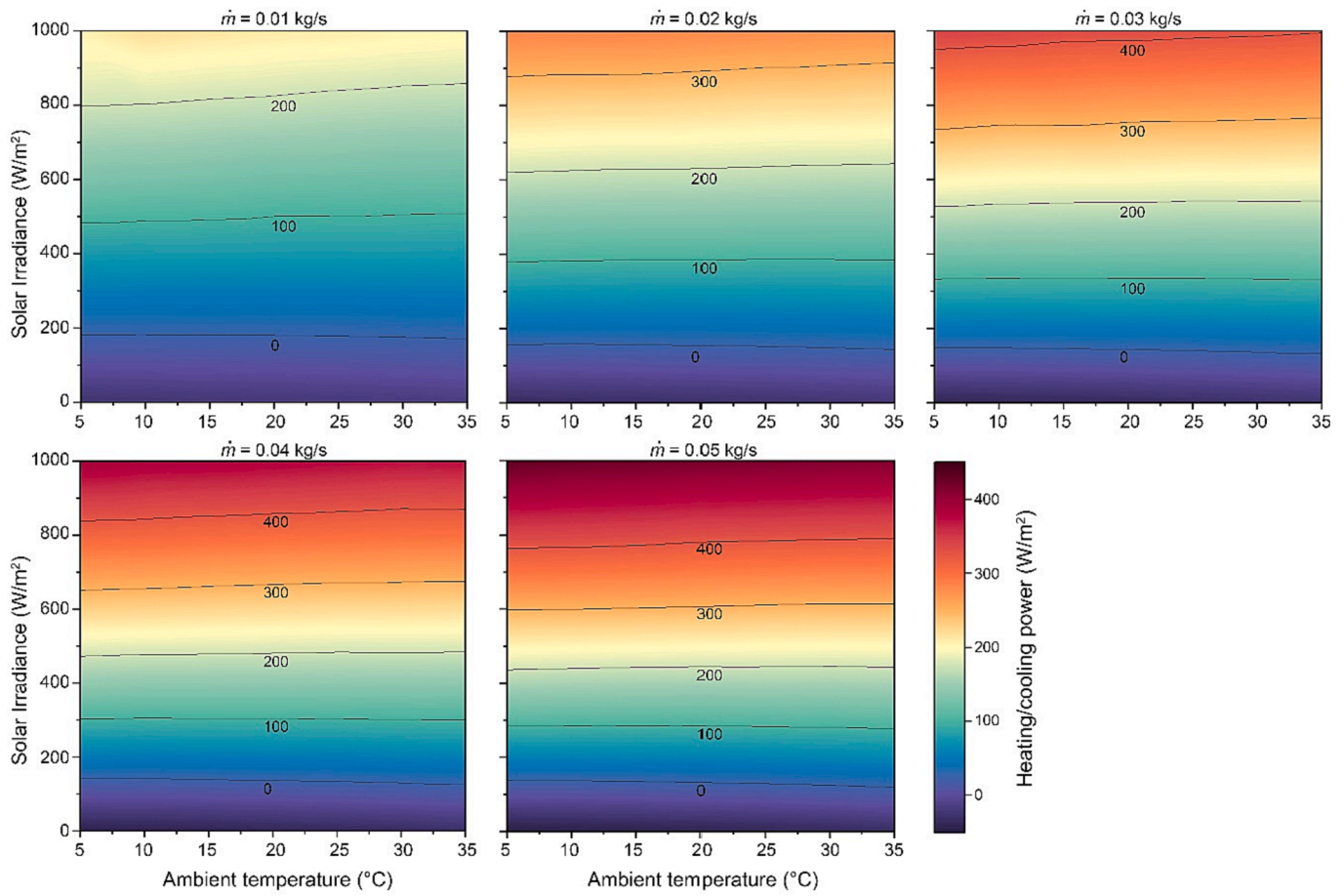


Fig. 15. Effect of ambient temperature and solar irradiance on the SHRC collector's performance with five different air mass flow rates.

displaying results that are more like minutely rather than hourly conditions.

Furthermore, the simulation results of the small time step sizes (≤ 600 s) are converging. RMSD of the simulations results from the 600 s and 300 s, compared to the 60 s, are 3.1 % and 1.5 % respectively. However, using the 60 s (1 min) time step size for the annual simulations used in the energy-saving analysis is impractical. Hence, the 300 s and 600 s time step sizes are the best options, since they can resemble the simulation results with the 60 s time step size. However, when looking at the thermal efficiency data, the 600 s time step size still has the characteristic of the large time step, i.e., that it has a sudden change in the afternoon. Thus, in this regard, the 300 s one is the more feasible time step size to use for reliability and speed of calculation.

c. Differences between 3-dimensional and 2-dimensional simulation results.

From the time step size analysis, the preferred time step size for the SHRC transient simulation is chosen. However, a 3-dimensional (3D) CFD model may still be time-consuming for simulations involving an annual simulation. To shorten the simulation time of the annual energy-saving analysis, the geometry used in the model can be simplified into a 3D with a symmetry wall (3D-half) or a 2D geometry. The comparison of simulation results from the 3D-full, 3D-half, and 2D models are compared in Fig. 14. The figure shows the very close agreement in all parameters between the 3D full and 3D half, with 0.4 % RMSD between the two. As for the 2D model, it is seen that the model tends to overestimate the heating performance. This is because the 2D model assumes the heating condition in the middle of the SHRC collector to be uniform across its width. There will always be a gradation of temperature

distribution farther from the middle. Outlet temperature differences can be up to 4 °C higher in the 2D than in the 3D models, leading to a heating power gap of around 45 W/m². Nevertheless, the RMSD of the 2D model compared to the 3D-full model is 4.3 % and the plotting of all parameters in Fig. 14 shows no considerable differences in the hourly pattern. Thus, for this reason, 2D is considered reliable to be used in the annual energy-saving analysis.

4. Results and discussion

4.1. Parametric studies

a. The effect of solar irradiance, ambient temperature, and mass flow rate.

The performance of the SHRC collector is strongly influenced by ambient conditions, particularly ambient temperature and solar irradiance. Fig. 15 illustrates the impact of various ambient temperatures and solar irradiance levels on the heating and cooling power of the SHRC collector at five different air mass flow rates (\dot{m}). It is important to note that in this parametric study, Eq. (8) was used to estimate the sky temperature for parametric studies.

The figure shows that the heating power of the SHRC increases with solar irradiance and that the rate of increase is consistent across different ambient temperatures. However, a closer examination of the data reveals that in a higher solar irradiance, the collector's heating power tends to be better at low ambient temperature. As seen in Fig. 15, the lines of equal heating power tend to turn upward as the ambient temperature increases at solar irradiance > 700 W/m², and it is observed in all the tested mass flow rates. This shows that the same heating power

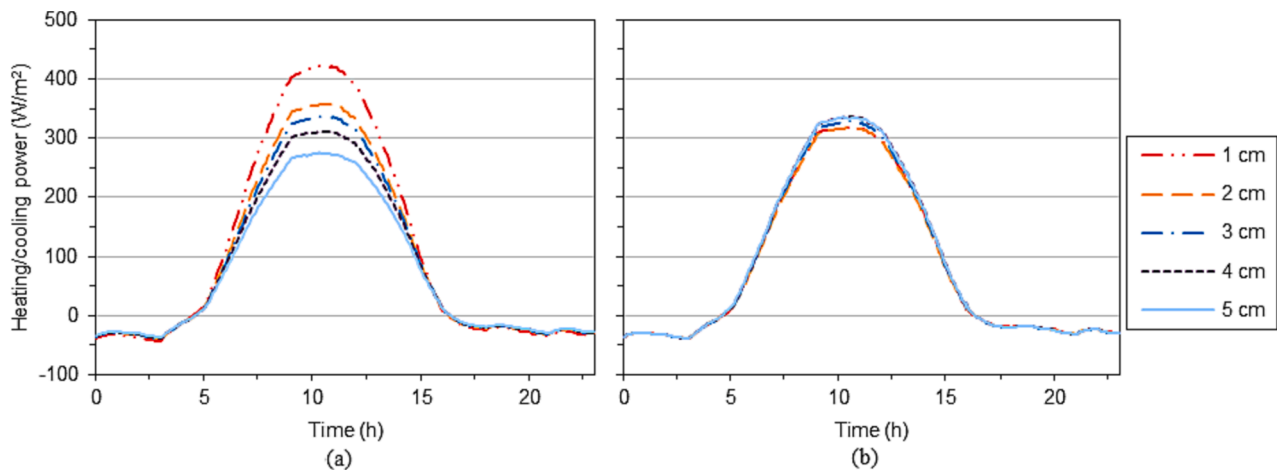


Fig. 16. (a) The effect of air duct heights (simulated with an air gap of 4 cm), and (b) the effect of air gap heights (simulated with an air duct of 3 cm) on the heating and cooling power of the SHRC collector (typical summer day of Isfahan (28-Jun.), $\dot{m} = 0.04$ kg/s).

can be achieved with less solar radiation at a lower temperature. Also, this effect is more evident for the smaller mass flow rates. On the contrary, in a lower solar irradiance, e.g., <300 W/m², the lines of equal heating power decline with the rise in ambient temperature. The effect is more apparent for the lower mass flow rates as well. This shows that

with solar irradiance less than 300 W/m², the higher ambient temperature means better heating performance.

Additionally, one notable point from the effect of solar irradiance on cooling power is that cooling occurs not only when the solar irradiance is 0 (i.e., during the night). It is deduced from Fig. 15 that the SHRC

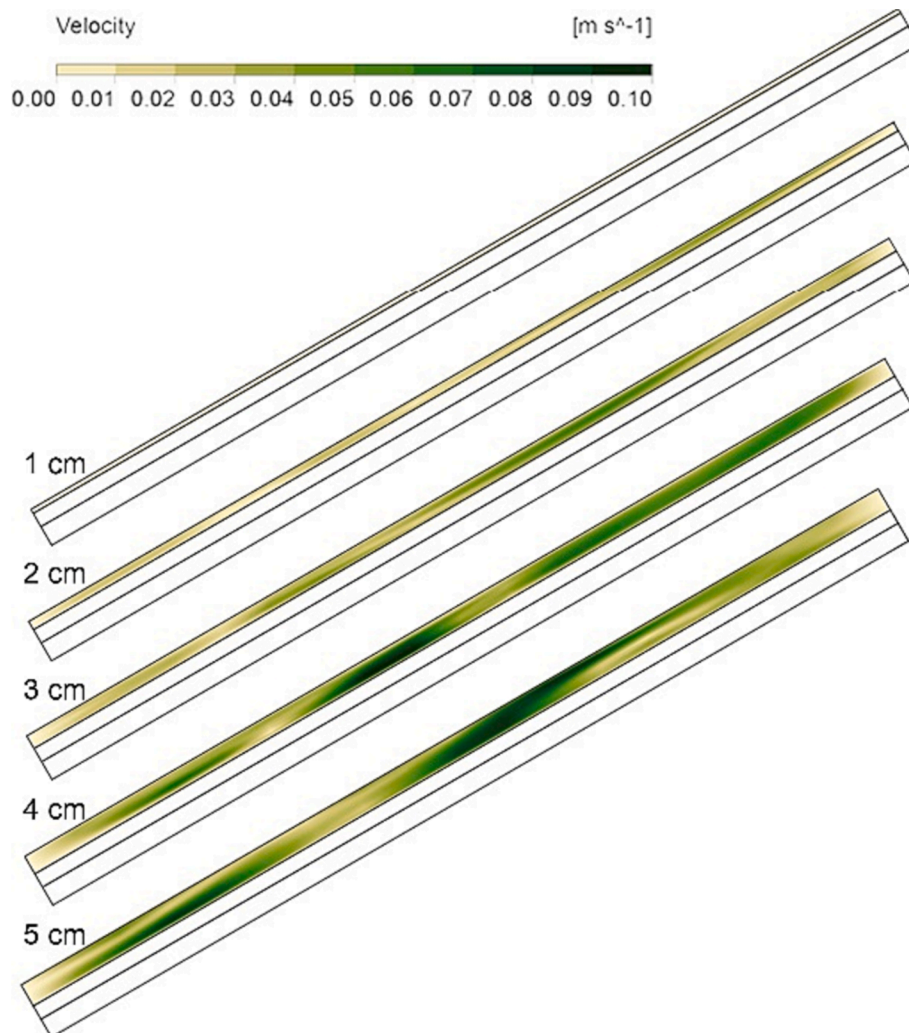


Fig. 17. Velocity contour of three representative air gaps for the same simulation as in Fig. 16 at 12p.m.

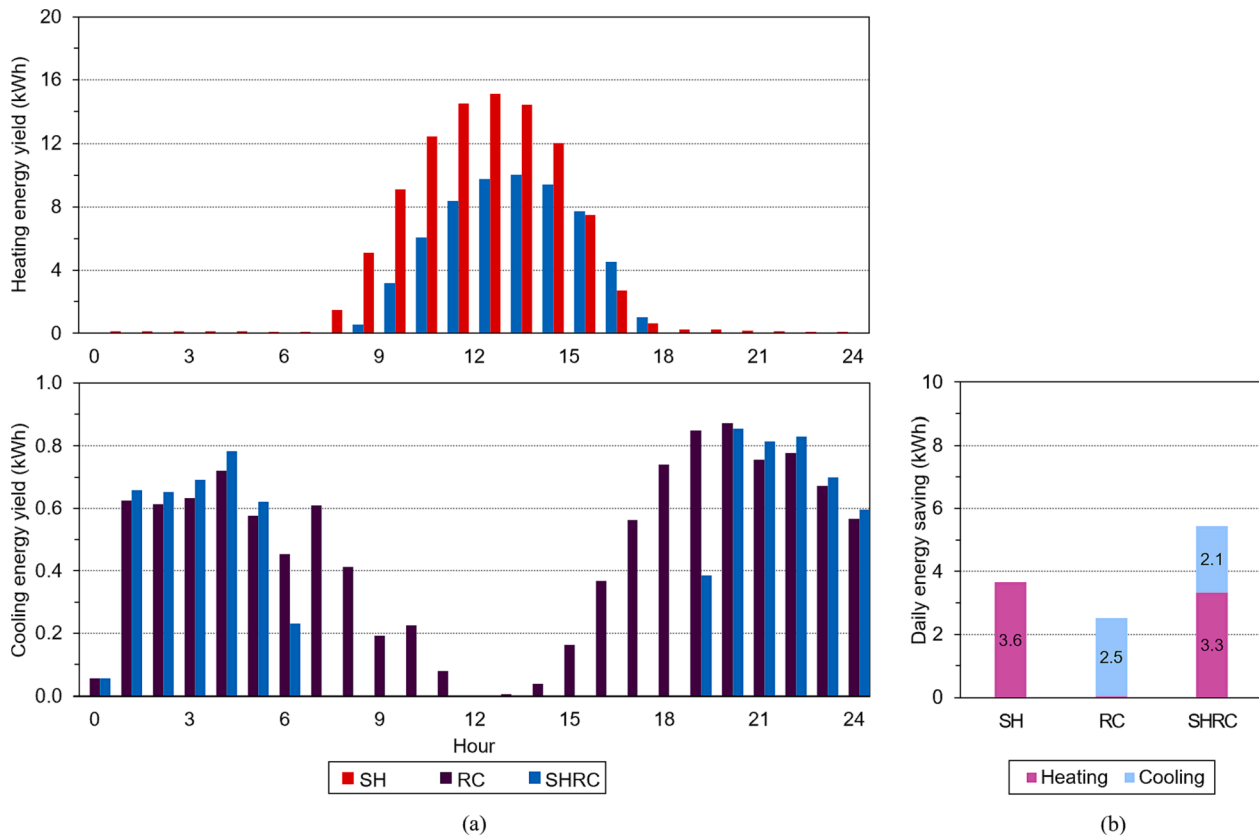


Fig. 18. Comparison between the (a) heating and cooling energy yield, based on typical winter (6-Jan) and summer (28 Jun) days in Isfahan ($A = 9.43 \text{ m}^2$, $\dot{m} = 0.04 \text{ kg/s}$), and (b) energy saving potential of SH, RC, SHRC, and near ideal SHRC collectors.

collector starts to give cooling power at solar irradiance below 100 W/m^2 . The solar irradiance level in which the cooling effect starts is higher at the low ambient temperature, and this is quite consistent in all mass flow rates. This means that it is easier for the SHRC collector to start to cool the air at the low ambient temperature, mainly because the sky emissivity formula in Eq. (8) gives a larger gap between the ambient and sky temperature at the lower ambient (or dew point) temperature.

In terms of the mass flow rate's effect, it is expected that the higher mass flow rate generates a better heating and cooling performance. However, the higher mass flow rates also result in higher pressure differences and thus greater fan power consumption. Therefore, the heating and cooling power provided by the SHRC collector in Fig. 15 is the adjusted value considering the fan power for each mass flow rate. At a mass flow rate of 0.01 kg/s , the SHRC collector can only achieve around 200 W/m^2 of heating and 28 W/m^2 of cooling power at best. Whereas, with the mass flow rate of 0.05 kg/s , the collector can provide more than 400 W/m^2 of heating and 50 W/m^2 cooling power. Also, the influence of ambient temperature on the collector's heating/cooling power is more pronounced at lower mass flow rates, as shown by the steeper contour line gradients in Fig. 15 for a mass flow rate of 0.01 kg/s compared to 0.02 kg/s . As the mass flow rate increases, the contour lines become more horizontal, indicating that ambient temperature has a lesser effect on the collector's heating/cooling power.

b. The effect of the air duct and air gap heights.

Besides the environmental conditions, the collector's design is also an influential factor for the heating/cooling power. Using the typical summer day in Isfahan, the effect of various air duct and air gap heights were simulated, and the results are summarised in Fig. 16. It is noteworthy that a smaller air duct means higher pressure is needed by the fan, and hence the fan will need more power to deliver the same mass

flow rate in the smaller air duct. Therefore, Fig. 16 shows the adjusted heating and cooling power after the fan power effect due to the increase in pressure is subtracted. The effect of air duct height is more apparent around noon time when the solar irradiance level is high. Thus, the optimal air duct design can be deduced by comparing mainly the heating performance during the daytime. As expected, the smaller air duct transfer heats more efficiently from the collector to the air, as Fig. 16a shows the superiority of the 1 cm air duct over the other larger heights. With a 1 cm air duct, the SHRC collector has 422.7 W/m^2 maximum heating power (at least 65.3 W/m^2 higher than the other air ducts) during the day and 43.6 W/m^2 maximum cooling power (or at least 4.3 W/m^2 higher than the other air ducts) at night.

Similarly, the effect of air gap height is also more obvious during the sunlit period. But, unlike the air duct, the heating/cooling power is not neatly correlated with the air gap height. Although large air gaps mean less conductive heat flux through the air, but potentially provide a space for the natural convection flow due to the temperature difference between the absorber/emitter and the PE cover. Hence, there is an optimal air gap height that maximises its thermal resistance but minimises the natural convection. Fig. 16b shows that the 1 cm and 2 cm air gaps have lesser heating power at noon, the 3 cm air gap has slightly better performance, and the 4 cm and 5 cm air gaps show the best results. But Fig. 16b also shows that there is hardly any difference in heating/cooling power between the 4 cm and 5 cm air gaps.

Detailed analysis of this conflicting tendency of the air to prevent conductive heat transfer and promote convective heat transfer can be done with the help of air velocity contours in the air gap. Fig. 17 depicts the velocity contours of different air gaps from the same simulations as in Fig. 16, taken specifically at 12p.m. It can be seen from the velocity contour that there is hardly any air movement in the 1 cm air gap, while there is some space in the 5 cm air gap where the air moves with a speed of 0.1 m/s or more. When looking at the temperature contour in Fig. 17,

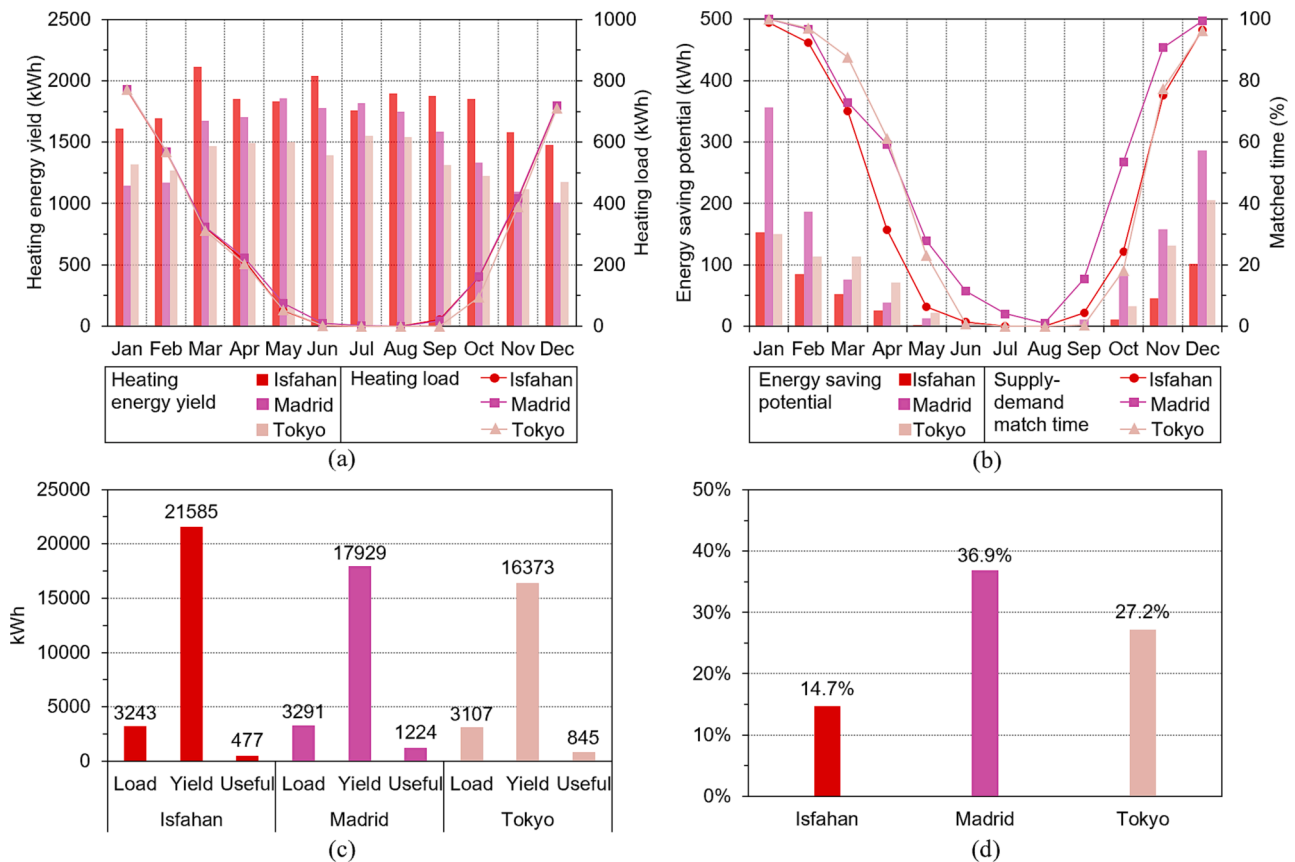


Fig. 19. (a) The monthly heating load and energy yield; (b) the monthly supply-demand time matching and energy saving potential; (c) the total annual heating load, yield, and useful/saved energy; and (d) the percentage of useful heating energy to the heating load ($A = 9.43 \text{ m}^2$, $\dot{m} = 0.04 \text{ kg/s}$).

this movement of air is the convection movement of hot air, taking heat from the absorber to the PE cover. Thus, as Fig. 16b shows, the 5 cm air gap has slightly less (1.39 W/m^2 heating power than the 4 cm gap. Therefore, in this regard, the optimal air gap height that can be used for the energy-saving analysis is 4 cm.

4.2. Energy saving potential of the building-integrated SHRC collector

a. Comparison with the mono-functional SH and RC.

The SHRC collector is designed to offer an additional function for night-time cooling to the conventional SH collector. This additional function requires a different structure for the SHRC collector, which may impact its heating performance. Fig. 18 displays the comparison between the SH, RC, and SHRC collectors' energy yield for the typical winter and summer days of Isfahan. The simulations for the energy yield were done for the building-integrated system which consists of 5 collectors (9.43 m^2 collector area).

As expected, the heating energy yield of the SHRC collector is lower than the SH collector, and similarly, the cooling energy yield is also lower than the RC collector. The hourly differences in heating energy yield between the SH and SHRC collectors are wider as the solar irradiance peaks, as shown in Fig. 18. Likewise, the discrepancy in cooling energy yield between the RC and SHRC collectors is widened during the day. These discrepancies in heating and cooling energy yield from the SHRC collector compared to the SH and RC collectors are due to differences in the spectral properties of the three collectors. For instance, due to the low thermal emissivity of the SH collector, the collector is better at keeping heat than the SHRC collector with high thermal emissivity (see Fig. 18a). As a result, during the peak solar irradiance, the SH collector can collect more heating energy than the SHRC

collector. Also, the SH collector starts to lose heat from its surface later in the afternoon and picks up some heat earlier in the morning than the SHRC collector.

Moreover, with its high absorptivity/emissivity in the radiation outside the atmospheric window band, the SHRC collector also provides much less cooling energy than the RC collector during the daytime when the solar and sky radiations are strong (see Fig. 18a). However, at late night, the SHRC collector can release more heat from its surface due to its higher thermal absorptivity/emissivity in a broader band than the RC collector. Yet, this compensation still cannot make the total daily cooling energy yield of the SHRC collector better than the RC collector. The advantage of daytime cooling performance causes the total daily cooling energy yield of the RC collector at least 0.4 kWh more than the SHRC collector (Fig. 18b).

Nevertheless, Fig. 18a and b also reveal the advantage of the SHRC collector. On a typical winter day, the SH and SHRC collectors can deliver heating, while the RC collector barely provides any heating at all. On the other hand, on the typical summer days when cooling is needed, only the RC and SHRC collectors can supply cooling energy, while the SH does not perform (Fig. 18a). In this regard, the SHRC collector has the advantage of multi-seasonal performance over the SH and RC collectors. The daily heating and cooling energy yields by the SHRC collector in the typical winter and summer days are around 37.3% lower than SH and 31.9% lower than RC respectively. Compared to the non-existent heating energy provided by the RC collector in the winter, or cooling energy by the SH collector in the summer, the previous energy yield reduction is preferable.

The multi-seasonal advantage of the SHRC collector is best demonstrated by the combined heating and cooling savings achievable during the typical winter and summer periods. As depicted in Fig. 18b, the SH collector has the potential to save up to 3.6 kWh of heating energy on a

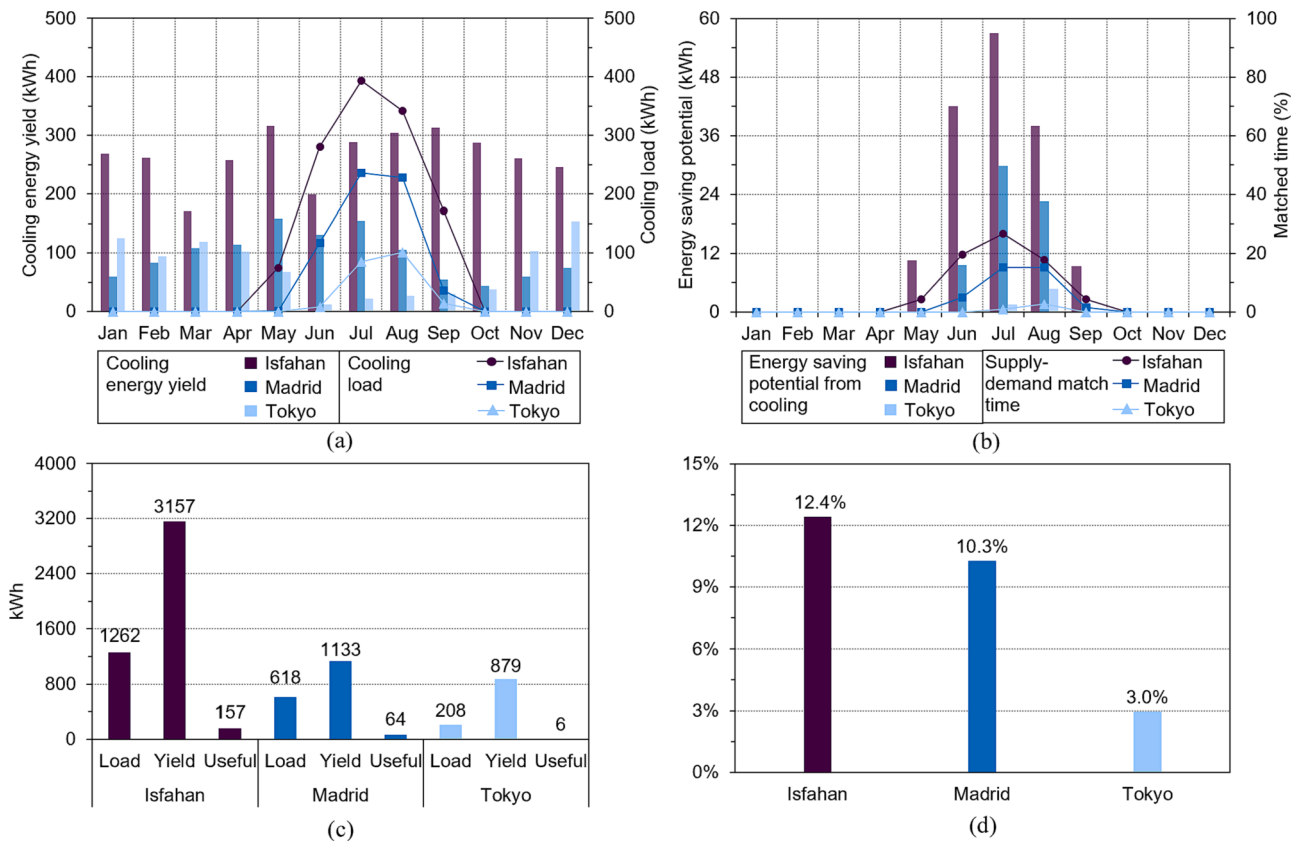


Fig. 20. (a) The monthly cooling load and energy yield; (b) the monthly supply-demand time matching and energy saving potential; (c) the total annual cooling load, yield, and useful/saved energy; and (d) the percentage of useful cooling energy to the cooling load ($A = 9.43 \text{ m}^2$, $\dot{m} = 0.04 \text{ kg/s}$).

typical winter day, while the RC collector can contribute up to 2.5 kWh of cooling energy savings on a typical summer day. However, when the daily heating and cooling energy savings are combined, the SHRC collector outperforms the two mono-functional collectors, yielding a total energy savings of 5.4 kWh. This finding confirms the multi-seasonal advantage of the SHRC collector.

b. Energy saving potential in different climates.

Since the SHRC collector performance is highly dependent on solar irradiance (for heating) and clear sky and humidity level (for cooling), its energy-saving potential in different climates must be different. To assess which climate condition is appropriate for the SHRC collector, Fig. 19 compares the heating load, energy yield, as well as potential savings from the SHRC collector in three different climates. The figures reveal the mismatching and the discrepancy in magnitude between the heating and cooling loads with the available energy. In Fig. 19a, the heating energy is available throughout the year roughly with a magnitude >1000 kWh per month in all three climates. This heating energy yield is used 100 % in the winter months, but because there is no heating load in the summer, the energy is wasted in the summer with 0 % of match time between the supply and demand (Fig. 19b).

In addition to that, Fig. 19c summarises the annual heating load, yield, and useful heating energy in the three climates. The SHRC collector provides a huge amount of heating energy yield in the three climates, which are 21,585 kWh in Isfahan, 17,929 kWh in Madrid, and 16,373 kWh in Tokyo. These results indicate the superiority of the SHRC collector performance in the two dryer climates, namely Isfahan and Madrid, compared to the humid climate in Tokyo. However, considering the differences in heating load between the climates, the percentage of yield and useful energy compared to the load can be seen as higher in Madrid (Csa climate) compared to Isfahan (BWk), and Tokyo (Cfa). Five

SHRC collectors in Madrid climate can reduce energy consumption for heating up to 36.9 %, while Isfahan and Tokyo can save up to 14.7 % and 27.2 % respectively (Fig. 19d).

Furthermore, Fig. 20 summarises the cooling load, as well as the available and useful cooling energy from the SHRC collector in the three climates. Like the heating, the cooling energy available also mismatches the cooling demand, as seen in Fig. 20a where the available cooling coincides with zero cooling load in the winter. But, unlike the heating energy that is 100 % useful during the heating season, the cooling energy from the SHRC collector cannot even achieve a 30 % match time during the cooling season (see Fig. 20b). This is because the SHRC collector provides cooling mostly at night, but the demand mostly occurs during the daytime. In other words, the mismatch between the cooling load and energy yield is not only seasonal but also diurnal. This condition is also responsible for the lower percentage of energy-saving potential from cooling compared to heating, as summarised by the annual cooling energy numbers shown in Fig. 20c. In the figure, the energy yields exceed the cooling loads in three climates. But this available cooling energy is again reduced by the mismatch time between the cooling load and energy yield. The percentage of useful cooling energy compared to the load is 12.5 % in Isfahan, 10.3 % in Madrid, and 3 % in Tokyo (Fig. 20d). This shows that the Isfahan climate is the most appropriate condition to optimally use the SHRC collector for cooling, in line with the weather data in Fig. 10 that shows the lower sky temperature in Isfahan compared to the other case study locations.

5. Conclusion

The importance of using renewable heating and cooling systems to reduce annual domestic energy expenses is rising due to global warming. Available renewable heating and cooling systems are usually standalone single-functional devices, which can be costly to install and maintain.

For a climate region with heating and cooling seasons, a dual-functional device for renewable heating and cooling might be more convenient. This study has examined such a device in the form of an SHRC collector. Unlike the conventional SH collector which has high absorptivity in the solar band (0.2–3 μm), the SHRC collector has high absorptivity in the solar band and infrared band (especially the atmospheric window band). Also, the glass cover that originally protects the SH collector from convective heat loss is changed to a PE cover that is transparent for infrared radiation. These adjustments in the spectral properties of the collector and the cover make the daytime-only solar collector a whole-day SHRC collector.

The sensitivity analyses of the CFD model in Ansys Fluent provided an appropriate model for the annual energy-saving analysis of the SHRC collector. Additionally, EnergyPlus simulations were also conducted to provide the energy-saving analysis, with the case study building developed from the IEA EBC Annex 58. The CFD simulation results comparing the performance of the conventional SH, RC, and SHRC collectors reveal the advantage of the dual-functional collector in the multi-seasonal performance. Using the typical winter and summer days of Isfahan, the simulations show a 5.4 kWh combined heating and cooling daily energy savings by the SHRC collector, compared to only 3.6 kWh and 2.5 kWh by the SH and RC collector respectively.

Furthermore, with a 100 m² case study building and 9.43 m² of collector area, the building-integrated SHRC collector was simulated in three different locations with various climate types. The results demonstrate that the SHRC collector delivers heating and cooling energy the most in the Mediterranean climate like Madrid. This is indicated by the 36.9 % heating energy saving by the building-integrated SHRC collector in Madrid annually, compared to 27.2 % in the humid subtropical climate of Tokyo, and 14.7 % in Isfahan. The building-

integrated SHRC collector can also save 12.5 % of energy for cooling in Isfahan, compared to 10.3 % in Madrid and, only 3.0 % in Tokyo. The combined heating and cooling energy savings by the SHRC collector annually are 32.7 % in Madrid, 25.5 % in Tokyo, and 14.0 % in Isfahan.

Nevertheless, this study has some limitations such as the use of a 2D model in estimating the energy saving potential which can overestimate the heating and underestimate the cooling energy savings. Also, the annual energy saving potential figures can still be improved considering the mismatch between the time in which the heating and cooling are available with the loads. Studies on the use of energy storage mechanisms or heating and cooling load management can further improve the utility of this dual-functional SHRC collector.

Declaration of Competing Interest

The authors declare that they have no known competing financial interests or personal relationships that could have appeared to influence the work reported in this paper.

Data availability

Data will be made available on request.

Acknowledgements

This research was supported by a PhD studentship (Reference number: S-2401/LPDP.4/2019) funded by the Indonesia Endowment Fund for Education (Lembaga Pengelola Dana Pendidikan), Ministry of Finance, Republic of Indonesia, and the H2020 Marie Skłodowska-Curie Actions-Individual Fellowships (Grant number: 842096).

Appendix A. Ansys Fluent settings

- General: pressure-based solver, transient simulation.
- Energy: On.
- Viscous model: Laminar.
- Radiation model: Discrete ordinates with 4 radiation bands (Band 0: 0.2–3 μm; Band 1: 3–8 μm; Band 2: 8–13 μm; Band 3: 13–25 μm).
- Materials.

Material	Thermal properties		
	Thermal conductivity (W·m ⁻¹ ·K ⁻¹)	Density (kg·m ⁻³)	Specific heat capacity (J·kg ⁻¹ ·K ⁻¹)
Air	Piecewise linear 250 K: 0.0223300 K: 0.0263350 K: 0.03400 K: 0.0338	Incompressible ideal gas law	Piecewise linear 250 K: 1006300 K: 1007350 K: 1009400 K: 1014
Insulation	0.033	38	1400
Absorber/emitter (aluminium)	202.4	2719	871
PE film	910	910	1900
Glass	1.38	2203	703

- Cell Zone Conditions:
 - o Operating pressure: 101325 Pa
 - o Gravity in Y direction −9.81 m/s²

Cell zone name	Type (Material)	Condition
Air gap	Fluid (Air)	Participates in Radiation
Air duct	Fluid (Air)	Participates in Radiation
Insulation	Solid (Insulation)	Participates in Radiation

- Boundary condition

Boundary name	Type (Material)	Thermal Boundary conditions	Radiation Boundary Conditions
Inlet	Velocity inlet	Temperature: T_{in}	0
Outlet	Pressure outlet	Backflow temperature: T_{amb}	0
Cover	Wall (PE cover)	Mixed <ul style="list-style-type: none"> Heat transfer coefficient: h_{wind} Free stream temperature: T_{amb} External emissivity: 1 External radiation temperature: T_{sky} 	Internal emissivity Band 0: 0.05 Band 1: 0.05 Band 2: 0.05 Band 3: 0.05
Side insulation	Wall (Insulation)	Convection <ul style="list-style-type: none"> Heat transfer coefficient: h_{wind} Free stream temperature: T_{amb} 	Internal emissivity Band 0: 0.7 Band 1: 0.9 Band 2: 0.9 Band 3: 0.9
Back insulation	Wall (PE cover)	Convection <ul style="list-style-type: none"> Heat transfer coefficient: h_{wind} Free stream temperature: T_{amb} 	Internal emissivity Band 0: 0.7 Band 1: 0.9 Band 2: 0.9 Band 3: 0.9
Absorber/emitter	Two-sided Wall (Aluminium)	Coupled; External heat sources in Eq. (12), namely $q_{sol-a/c} + q_{rad}$, are inputted in the Heat Generation Rate entry-box*	Internal emissivity Band 0: 0.92 Band 1: 0.51 Band 2: 0.84 Band 3: 0.54
The inner side of the insulation	Two-sided Wall (Insulation)	Coupled	Internal emissivity Band 0: 0.7 Band 1: 0.9 Band 2: 0.9 Band 3: 0.9

*Because the Heat Generation Rate input box uses a volumetric unit, W/m^3 , we need to convert the external heat source equation of the surfaces to have the required unit. We did this by dividing the heat equation by the thickness of the wall and inputting that thickness into the Wall Thickness input box.

• Solution Methods

- o Pressure-Velocity Coupling Scheme: Coupled
- o Spatial Discretization:
 - Gradient: Least Square Cell-Based
 - Pressure: PRESTO!
 - Momentum: Second Order Upwind
 - Energy: Second Order Upwind
 - Discrete Ordinates: First Order Upwind
 - Transient Formulation: First Order Implicit

• Monitors

- o Residual checking:

continuity	1×10^{-6}
x-velocity	1×10^{-6}
y-velocity	1×10^{-6}
energy	1×10^{-6}
k	1×10^{-6}
epsilon	1×10^{-6}
DO-intensity	1×10^{-6}

o Reported parameters for convergence checking

- Outlet and absorber/emitter temperatures
- Specific heat capacity at the outlet
- Mass flow rate
 - Running simulation: Time step size: 300 s

References

- [1] S.J. Brown, Future changes in heatwave severity, duration and frequency due to climate change for the most populous cities, *Weather Clim Extrem.* 30 (2020), 100278, <https://doi.org/10.1016/j.wace.2020.100278>.
- [2] K. Sun, W. Zhang, Z. Zeng, R. Levinson, M. Wei, T. Hong, Passive cooling designs to improve heat resilience of homes in underserved and vulnerable communities, *Energy Build.* 252 (2021) 111383.
- [3] Nasa Earth Observatory, Heatwaves and Fires Scorch Europe, Africa, and Asia, (2022). earthobservatory.nasa.gov.
- [4] Is the globe prepared? 2022 phys.org/news/2022-08-extreme-climate-globe.html.
- [5] A. Velashjerdi Farahani, J. Jokisalo, N. Korhonen, K. Jylhä, K. Ruosteenoja, R. Kosonen, Overheating risk and energy demand of nordic old and new apartment buildings during average and extreme weather conditions under a changing climate, *Applied Sciences (switzerland)*. 11 (9) (2021) 3972.
- [6] A.M.R. Nishimwe, S. Reiter, Estimation, analysis and mapping of electricity consumption of a regional building stock in a temperate climate in Europe, *Energy Build.* 253 (2021) 111535.
- [7] K.J. Chua, S.K. Chou, W.M. Yang, J. Yan, Achieving better energy-efficient air conditioning - A review of technologies and strategies, *Appl Energy*. 104 (2013) 87–104, <https://doi.org/10.1016/j.apenergy.2012.10.037>.
- [8] D. Yan, X. Zhou, J. An, X. Kang, F. Bu, Y. Chen, Y. Pan, Y. Gao, Q. Zhang, H. Zhou, K. Qiu, J. Liu, Y. Liu, H. Li, L. Zhang, H. Dong, L. Sun, S. Pan, X. Zhou, Z. Tian, W. Zhang, R. Wu, H. Sun, Y. Huang, X. Su, Y. Zhang, R. Shen, D. Chen, G. Wei, Y. Chen, J. Peng, DeST 3.0: A new-generation building performance simulation platform, *Build Simul.* 15 (2022) 1849–1868, <https://doi.org/10.1007/s12273-022-0909-9>.
- [9] Eurostat, Energy consumption in households, (2022). ec.europa.eu/eurostat/statistics-explained.
- [10] Climate Change Committee, The sixth carbon budget: the UK's path to net zero, (2020).
- [11] J. Zhang, T. Zhu, Systematic review of solar air collector technologies: Performance evaluation, structure design and application analysis, *Sustainable Energy Technologies and Assessments*. 54 (2022), 102885, <https://doi.org/10.1016/j.seta.2022.102885>.
- [12] A. Zairi, A. Mejedoub Mokhtari, S. Menhoudj, Y. Hammou, K. Dehina, M.-H. Benzaama, Study of the energy performance of a combined system: Solar thermal collector – Storage tank – Floor heating, for the heating needs of a room in Maghreb climate, *Energy Build.* 252 (2021) 111395.
- [13] SolarWall, SolarWall Systems, (2022). www.solarwall.com.
- [14] L. Xu, C. Luo, J. Cai, J. Ji, L. Dai, B. Yu, S. Huang, Modeling and analysis of a dual-channel solar thermal storage wall system with phase change material in hot

- summer and cold winter area, *Build Simul.* 15 (2022) 179–196, <https://doi.org/10.1007/s12273-021-0805-8>.
- [15] M. Hoffman, K. Rodan, M. Feldman, D.S. Saposnik, Solar heating using common building elements as passive systems, *Solar Energy.* 30 (3) (1983) 275–287.
- [16] N.I. Dawood, J.M. Jalil, M.K. Ahmed, Investigation of a novel window solar air collector with 7-moveable absorber plates, *Energy.* 257 (2022), 124829, <https://doi.org/10.1016/j.energy.2022.124829>.
- [17] W. Li, A. Subiantoro, I. McClew, R.N. Sharma, CFD simulation of wind and thermal-induced ventilation flow of a roof cavity, *Build Simul.* 15 (2022) 1611–1627, <https://doi.org/10.1007/s12273-021-0880-x>.
- [18] S. Jafari, V. Kalantar, Numerical simulation of natural ventilation with passive cooling by diagonal solar chimneys and windcatcher and water spray system in a hot and dry climate, *Energy Build.* 256 (2022) 111714.
- [19] S. Rasheed, M. Ali, H. Ali, N.A. Sheikh, Experimental evaluation of indirect evaporative cooler with improved heat and mass transfer, *Appl Therm Eng.* 217 (2022), 119152, <https://doi.org/10.1016/j.applthermaleng.2022.119152>.
- [20] Q. Liu, C. Guo, Z. Wu, Y. You, Y. Li, Heat and mass transfer model optimization and annual energy efficiency analysis for energy recovery indirect evaporative cooling, *Build Simul.* 15 (2022) 1353–1365, <https://doi.org/10.1007/s12273-021-0868-6>.
- [21] M. Hu, B. Zhao, Suhendri, X. Ao, J. Cao, Q. Wang, S. Riffat, Y. Su, G. Pei, Applications of radiative sky cooling in solar energy systems: Progress, challenges, and prospects, *Renewable and Sustainable Energy Reviews.* 160 (2022) 112304.
- [22] S. Fan, W. Li, Photonics and thermodynamics concepts in radiative cooling, *Photonics and Thermodynamics Concepts in Radiative Cooling* 16 (3) (2022) 182–190.
- [23] R. Miao, X. Hu, Y. Yu, Y. Zhang, M. Wood, G. Olson, Experimental study of a newly developed dual-purpose solar thermal collector for heat and cold collection, *Energy Build.* 252 (2021) 111370.
- [24] S.N. Bathgate, S.G. Bosi, A robust convection cover material for selective radiative cooling applications, *Solar Energy Materials and Solar Cells.* 95 (2011) 2778–2785, <https://doi.org/10.1016/j.solmat.2011.05.027>.
- [25] M. Hu, Suhendri, B. Zhao, X. Ao, J. Cao, Q. Wang, S. Riffat, Y. Su, G. Pei, Effect of the spectrally selective features of the cover and emitter combination on radiative cooling performance, *Energy and Built Environment.* 2 (3) (2021) 251–259.
- [26] P. Strachan, K. Svehla, M. Kersken, I. Heusler, Reliable building energy performance characterisation based on full scale dynamic measurements, *Annex.* 58 (2016) 5.
- [27] B. Zhao, X. Ao, N. Chen, Q. Xuan, M. Hu, G. Pei, A spectrally selective surface structure for combined photothermic conversion and radiative sky cooling, *Frontiers in Energy.* 14 (2020) 882–888, <https://doi.org/10.1007/s11708-020-0694-z>.
- [28] M. Hu, B. Zhao, Suhendri, J. Cao, Q. Wang, S. Riffat, Y. Su, G. Pei, Extending the operation of a solar air collector to night-time by integrating radiative sky cooling: A comparative experimental study, *Energy.* 251 (2022) 123986.
- [29] D. Li, X. Liu, W. Li, Z. Lin, B. Zhu, Z. Li, J. Li, B.o. Li, S. Fan, J. Xie, J. Zhu, Scalable and hierarchically designed polymer film as a selective thermal emitter for high-performance all-day radiative cooling, *Scalable and Hierarchically Designed Polymer Film as a Selective Thermal Emitter for High-Performance All-Day Radiative Cooling* 16 (2) (2021) 153–158.
- [30] ANSYS FLUENT 13, *ANSYS Fluent Theory Guide*, ANSYS Inc., USA. 15317 (2013) 724–746.
- [31] Ansys®, *ANSYS Fluent, R1, Help System, Fluent User's Guide*, ANSYS Inc, Solution Mode, 2021, p. 2021.
- [32] M. Hu, B. Zhao, Suhendri, J. Cao, Q. Wang, S. Riffat, Y. Su, G. Pei, Quantitative characterization of the effect of inclination angle on flat-plate radiative cooling performance in buildings, *Journal of Building, Engineering.* 59 (2022) 105124.
- [33] R. Tang, Y. Etzion, I.A. Meir, Estimates of clear night sky emissivity in the Negev Highlands, Israel, *Energy Convers Manag.* 45 (2004) 1831–1843, <https://doi.org/10.1016/j.enconman.2003.09.033>.
- [34] L. Evangelisti, C. Guattari, F. Asdrubali, On the sky temperature models and their influence on buildings energy performance: A critical review, *Energy Build.* 183 (2019) 607–625, <https://doi.org/10.1016/j.enbuild.2018.11.037>.
- [35] J. Watmuff, W. Charters, D. Proctor, Solar and wind induced external coefficients - Solar collectors, *Cooperation Mediterranee Pour L'energie Solaire.* 1 (1977) 56.
- [36] P. Strachan, K. Svehla, I. Heusler, M. Kersken, Whole model empirical validation on a full-scale building, *J Build Perform Simul.* 9 (2016) 331–350, <https://doi.org/10.1080/19401493.2015.1064480>.
- [37] M. Kottek, J. Grieser, C. Beck, B. Rudolf, F. Rubel, World map of the Köppen-Geiger climate classification updated, *Meteorologische Zeitschrift.* 15 (3) (2006) 259–263.
- [38] ASHRAE, ANSI/ASHRAE Standard 55-2020 Thermal Environmental Conditions for Human Occupancy, (2020).
- [39] L.K. Lawrie, D.B. Crawley, *Development of Global Typical Meteorological Years (TMYx)*, (2022). <http://climate.onebuilding.org>.
- [40] R. Liggett, M. Milne, *Climate Consultant* 6 (2021).
- [41] ASHRAE, ANSI/ASHRAE/IES Standard 90.2 2018 Energy-Efficient Design of Low-Rise Residential Buildings, (2018).
- [42] B.L.S. LLC, *EnergyPlus Version 8.6 Documents*, (2022). bigladdersoftware.com.
- [43] H. Bahaidarah, A. Subhan, P. Gandhidasan, S. Rehman, Performance evaluation of a PV (photovoltaic) module by back surface water cooling for hot climatic conditions, *Energy.* 59 (2013) 445–453, <https://doi.org/10.1016/j.energy.2013.07.050>.